ELSEVIER

Chemical Geology 211 (2004) 237–260

CHEMICAL GEOLOGY
INCLUDING
ISOTOPE GEOSCIENCE

www.elsevier.com/locate/chemgeo

Correlations between chemical and age domains in monazite, and metamorphic reactions involving major pelitic phases: an integration of ID-TIMS and SHRIMP geochronology with Y–Th–U X-ray mapping

H. Daniel Gibson[a,*], Sharon D. Carr[a,1], Richard L. Brown[a,1], Michael A. Hamilton[b,2]

[a]*Ottawa–Carleton Geoscience Centre, Department of Earth Sciences, Carleton University, Ottawa, Ontario, Canada K1S 5B6*
[b]*J.C. Roddick Ion Microprobe Lab, Geological Survey of Canada, Ottawa, Ontario, Canada K1A 0E8*

Received 6 August 2003; accepted 11 June 2004

Abstract

Chemical mapping and in situ U–Th–Pb analyses reveal a link between age domains and zones of relative yttrium (Y) depletion or enrichment within monazite crystals and are correlated with metamorphic reactions involving garnet. Conventional, small-fraction isotope dilution thermal ionization mass spectrometry (ID-TIMS) and sensitive high-resolution ion microprobe (SHRIMP) techniques were utilized to measure U–Th–Pb isotopic compositions in metamorphic monazite from pelitic rocks of the southern Canadian Cordillera. Monazite ID-TIMS data from individual samples commonly demonstrate a 2 to 25 Ma range in U–Pb ages. This is difficult to reconcile using conventional regression techniques due to complexities such as excess ^{206}Pb or bulk mixing of discrete age domains. Backscattered electron (BSE) imaging and X-ray elemental mapping for Y, Th, and U revealed complex internal zonation within many of the monazite crystals and served as a guide for detailed, in situ (~30 μm) isotopic analysis using the SHRIMP. The Y maps generally provided the clearest indication of growth or recrystallization domains and were critical for targeting SHRIMP analysis because these relationships were not always clear in BSE, U, and Th images. Moreover, the Y domains consistently correlated with distinct age domains, with up to three or more in some crystals. These data clearly illustrate the cause of age dispersion within the analyzed monazite grains and demonstrate the significance of multiple age domains in metamorphic monazite that may be irreconcilable or misinterpreted when using conventional dating techniques such as ID-TIMS.

* Corresponding author. Present address: Department of Earth Sciences, Simon Fraser University, Burnaby, British Columbia, Canada VSA 1S6. Tel.: +1 604 291 5387; fax: +1 604 291 4198.

E-mail addresses: hdgibson@sfu.ca (H.D. Gibson), scarr@ccs.carleton.ca (S.D. Carr), rlbrown@rideau.net (R.L. Brown), mahamilton@geology.utoronto.ca (M.A. Hamilton).

[1] Fax: +1 613 520 2569.

[2] Present address: Department of Geology, University of Toronto, Toronto, Ontario, Canada M5S 3B1. Fax: +1 416 978 3938.

0009-2541/$ - see front matter © 2004 Elsevier B.V. All rights reserved.
doi:10.1016/j.chemgeo.2004.06.028

Recent studies have investigated the interaction between accessory minerals such as monazite and major pelitic phases throughout a metamorphic event. Researchers have begun to focus on the partitioning of Y between monazite and garnet because it is highly compatible in both phases. Due to its greater volume, garnet exerts considerable control over the Y budget available during metamorphism in pelitic rocks. Consequently, this is reflected in the production and consumption of monazite, as it is sensitive to the availability of Y, and is preserved as internal zones of relative Y enrichment or depletion. Thus, precise ages of contrasting Y domains within monazite provided by in situ ion probe analysis may be correlated with metamorphic reactions involving garnet and assigned to points along the *P–T* path.
© 2004 Elsevier B.V. All rights reserved.

Keywords: Monazite; Metamorphism; U–Th–Pb geochronology; ID-TIMS; SHRIMP; Chemical mapping

1. Introduction

Previous studies have demonstrated that monazite (Ce, La, Th, PO_4) is perhaps the most useful radiogenic mineral for providing metamorphic age constraints in amphibolite- to granulite-facies terranes (e.g., Parrish, 1990; Spear and Parrish, 1996; Hawkins and Bowring, 1999; Foster et al., 2002; Kohn and Malloy, 2003; Pyle and Spear, 2003). This is due to monazite's common occurrence, especially in metapelites, (Overstreet, 1967), high concentrations of radiogenic Pb vs. low common Pb (Heaman and Parrish, 1991), and resistance to thermally induced volume Pb diffusion (e.g., DeWolf et al., 1993; Smith and Giletti, 1997; Zhu et al., 1997; Braun et al., 1998; Cocherie et al., 1998; Crowley and Ghent, 1999; Zhu and O'Nions, 1999b; Cherniak et al., 2002). However, the interpretation of U–Th–Pb ages is often made difficult by a number of complexities that affect the isotopic systematics of monazite. For instance, unsupported ^{206}Pb in young monazite (Schärer, 1984), samples with significant age dispersion (Foster et al., 2002, and references therein), and hydrothermal alteration (Poitrasson et al., 1996, 2000) can render conventional isotope dilution thermal ionization mass spectrometry (ID-TIMS) U–Pb data sets meaningless or result in erroneous conclusions. Even when innovative in situ dating techniques were utilized (e.g., DeWolf et al., 1993; Harrison et al., 1995; Zhu et al., 1997; Cocherie et al., 1998), ambiguities persisted because the assignment of monazite ages to specific points along the *P–T* path of a metamorphic assemblage remained equivocal. Moreover, there continued to be uncertainty as to what part of the metamorphic cycle was actually dated such as prograde vs. retrograde, heating vs. cooling, or a hydrothermal event. Clearly, determination of the involvement of monazite production and/or consumption in metamorphic reactions is of paramount importance.

Fortunately, a number of investigations have improved our understanding of monazite. These include systematic studies of monazite occurrence in pelitic assemblages over a broad range of metamorphic grade (e.g., Smith and Barreiro, 1990; Kingsbury et al., 1993; Ferry, 2000; Rubatto et al., 2001; Wing et al., 2003), and insights into metamorphic reactions involving monazite based on textural observations, accessory assemblages, and thermodynamic considerations (e.g., Bingen et al., 1996; Pan, 1997; Ferry, 2000; Foster et al., 2000, 2002; Pyle and Spear, 2000a, 2003; Kohn and Malloy, 2003; Wing et al., 2003). These studies have elucidated the interaction between accessory monazite and major phases throughout a metamorphic event, and more specifically the partitioning of Y between these phases (e.g., Bea and Montero, 1999; Foster et al., 2000, 2002; Pyle et al., 2001; Pyle and Spear, 2003). They have established that garnet exerts considerable control over the Y budget available during metamorphism in pelitic rocks. Moreover, production and consumption of monazite is sensitive to the availability of Y, and is reflected internally in preserved Y zones. Constraining the ages of these Y zones should provide detailed chronologic information that can be applied to the *P–T* evolution of a metamorphic assemblage. This concept was investigated by Foster et al. (2002) using laser ablation multicollector inductively coupled plasma mass spectrometry (LA-MC-ICPMS) and electron microprobe (EMP) chemical analysis. However, for Mesozoic and younger monazite the sensitivity of the LA-MC-ICPMS required rastering of the

beam over a substantial area and depth (x–y–z= ~60×50×15 μm) of the analyzed crystal, usually across Y zone boundaries. Nevertheless, Foster et al. were able to demonstrate the link between Y zones and age domains and propose correlations with metamorphic reactions involving garnet.

This study builds upon these innovative contributions by integrating Y, Th, and U chemical mapping of monazite with high precision in situ sensitive high-resolution ion microprobe (SHRIMP) U–Th–Pb analysis. Two important distinctions regarding this study are worth noting: (1) To help guide ion beam placement, chemical maps were generated prior to the SHRIMP analysis, not after as was the case for most other similar studies. (2) The SHRIMP spots were limited to ~30-μm diameter and ~2-μm depth. This method afforded the best chance to date specific Y zones without inadvertent overlap with adjacent domains. The results below indicate that distinct zones of relative Y depletion or enrichment in metamorphic monazite correspond with discrete age domains. The dated Y domains are correlated with metamorphic reactions involving major pelitic phases and monazite based mainly on the work of Foster et al. (2000, 2002), Pyle et al. (2001) and Pyle and Spear (2003).

2. Geologic setting

The study area is composed of late Proterozoic to Paleozoic metasedimentary and metavolcanic rocks of the northern Selkirk Mountains, situated in the southern Omineca belt of the Canadian Cordillera (Fig. 1a and b). These rocks were initially deposited along the western paleo-margin of the North American craton (Monger et al., 1982). During Middle Jurassic to Paleocene contraction they were displaced northeastward ~250–300 km (e.g., Price and Mountjoy, 1970; Brown et al., 1993; Parrish, 1995) as part of the Selkirk allochthon (Read and Brown, 1981). During this time the allochthon is interpreted to have experienced protracted and diachronous internal deformation and metamorphism (Parrish, 1995). Subsequent Tertiary normal faulting along the Columbia River and Okanagan Valley fault systems has dissected and exposed all levels of the allochthon.

The complexly deformed rocks within the northern Selkirk Mountains comprise at least three generations of superposed folding that have been metamorphosed at low to high grade (Brown and Tippett, 1978; Simony et al., 1980; Perkins, 1983; Leatherbarrow, 1981). Bounding the eastern flank of this region is the southern Rocky Mountain trench (SRMT, Fig. 1b), which is part of an orogen-scale tectonic lineament that trends northeast–southwest for more than 2300 km along the strike of the Canadian Cordillera. A zone of structural divergence from east to west across the northern Selkirk Mountains defines a regional-scale structure (Fig. 1c), termed the Selkirk fan (Wheeler, 1963, 1965; Price and Mountjoy, 1970; Brown and Tippett, 1978). The structural style of the eastern flank of the northern Selkirk Mountains consists of moderate, southwest dipping faults, fold axial planes, and transposition foliation. Shallow, northeast dipping structures characterize the western flank of the region, which is partly situated in the immediate hanging wall of the Columbia River fault (Fig. 1c), a northwest-striking, crustal-scale, Eocene normal-sense shear zone (Parrish et al., 1988). This fault separates upper amphibolite facies footwall rocks of the Monashee complex that includes autochthonous North American basement (see Armstrong et al., 1991; Parkinson, 1991; Crowley, 1999) from greenschist-facies rocks of the Selkirk allochthon within the Selkirk Mountains.

Sillimanite- and sillimanite-K-feldspar-grade rocks core the central part of the study area, and are flanked on either side by progressively lower-grade assemblages (Fig. 1b). A set of northwest trending regional isograds (Fig. 1b), parallel to the structural grain of the region have been established based on the appearance or disappearance of the index minerals chlorite, biotite, garnet, staurolite, kyanite, and sillimanite in pelites (Leatherbarrow and Brown, 1978; Leatherbarrow, 1981; Simony et al., 1980). The lowest grade, chlorite-in assemblage is located in the west flank of the study area, in the immediate hanging wall of the Columbia River fault (Fig. 1b). Northeastward, the metamorphic grade steadily increases to sillimanite-K-feldspar-melt near the fan axis, and then decreases to kyanite–staurolite-grade adjacent to the SRMT.

Metamorphic pressures and temperatures across the region vary from west to east. On the basis of geothermobarometry, Leatherbarrow (1981) docu-

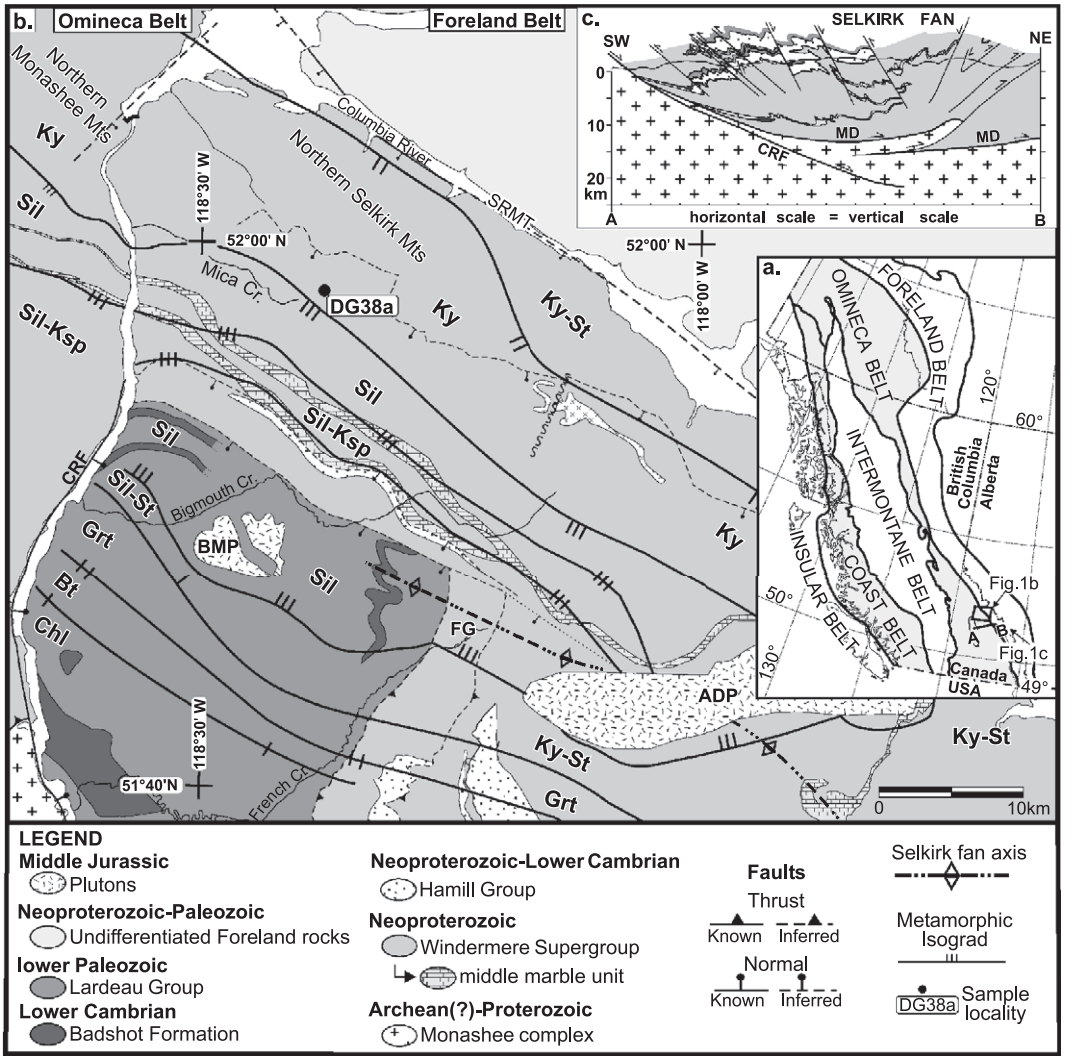

Fig. 1. (a) Morphogeologic belts of the Canadian Cordillera (modified after Wheeler and McFeely, 1991). A–B represents line of section for (c). (b) Generalized geologic map of the northern Selkirk Mountains illustrating lithostratigraphy, regional metamorphic isograds, major structures and location for sample DG38a. Compiled from Brown and Tippett (1978), Colpron et al. (1995), Leatherbarrow (1981), Perkins (1983), Poulton and Simony (1980), Raeside and Simony (1983), Simony et al. (1980), and Wheeler (1965). Abbreviations: ADP=Adamant pluton; BMP=Bigmouth pluton; FG=French Glacier; SRMT=southern Rocky Mountain trench; Mineral abbreviations for metamorphic zones after Kretz (1983). (c) Regional cross-section illustrating the geometry of the Selkirk fan in the northern Selkirk Mountains (modified after Brown et al., 1993). CRF=Columbia River fault; MD=Monashee décollement.

mented that in the southwest flank of the fan, in the vicinity of French Glacier (Fig. 1b), pressures and temperatures were 5 kbar and 500–550 °C (kyanite–staurolite zone). To the northeast within the sillimanite-K-feldspar zone, pressures were estimated to have reached at least 7 kbar and temperatures of 650 °C. Geothermobarometric studies to the north in the Mica Creek area agree well with Leatherbarrow. Ghent et al. (1979, 1982, 1983) estimated peak conditions of 540 to 700 °C and 5.6 to 7.2 kbar (lower P–T estimates for kyanite–staurolite zone, higher for sillimanite-K-feldspar zone).

Prior to this study, zircon U–Pb, and hornblende, muscovite and biotite $^{40}Ar/^{39}Ar$ age constraints for

deformation and metamorphism within the west flank of the fan were provided by Middle to Late Jurassic plutons (e.g., Shaw, 1980; Brown et al., 1992; Colpron et al., 1996). However, to the northeast of the fan axis, in the northernmost Selkirk and Monashee Mountains (Fig. 1c), zircon and monazite U–Pb and hornblende, muscovite and biotite $^{40}Ar/^{39}Ar$ and K/Ar data indicate that a significant episode of deformation and metamorphism (~5.5–8 kbar, 600–850 °C) also occurred in the Early Cretaceous to Tertiary (ca. 140–62 Ma) (Sevigny et al., 1989, 1990; Scammell, 1993; Digel et al., 1998; Crowley et al., 2000). Data from this contribution, as well as Gibson (2003) and Gibson et al. (in press), significantly refine the timing constraints for metamorphism and deformation across the Selkirk fan, and are used to reevaluate and revise thermotectonic models for the region (Gibson, 2003; Gibson et al., 2003, 2004, in preparation).

3. Analytical methods

Geochronologic methods included U–Pb ID-TIMS and U–Th–Pb SHRIMP analyses accompanied by backscattered electron (BSE) imaging and high-resolution Y–Th–U X-ray maps of metamorphic monazite from eight pelitic schist samples. Monazite crystals from all samples appear to have been variably affected by the complexities outlined in the introduction. However, for the sake of brevity, a detailed study of the sample that provided the greatest variety of chemical and age domains, DG38a, is presented in this contribution.

U–Pb ID-TIMS geochronology at Carleton University followed procedures outlined by Parrish et al. (1987). Monazite mineral separates were obtained by standard crushing, grinding, Rogers Gold™ table, heavy liquid, and Frantz™ magnetic separation techniques. When possible, the clearest, crack- and inclusion-free crystals were selected for analysis. Teflon® microcapsules (Parrish, 1987) were used for mineral dissolution and spiked with a mixed ^{233}U–^{235}U–^{205}Pb tracer (Parrish and Krogh, 1987). U–Pb isotopes were analyzed using a Finnigan MAT 261 multicollector mass spectrometer (as described by Roddick et al., 1987), and estimation of errors was based on numerical error propagation (Roddick, 1987). Decay constants used are those recommended by Steiger and Jäger (1977). Discordia lines through the analyses were calculated using a York (1969) regression. Typically, procedural U blanks were less than 5 pg and Pb blanks less than 10 pg. Common Pb corrections were made assuming model Pb compositions derived from the growth curves of Stacey and Kramers (1975).

For in situ analysis, monazite crystals were set in an epoxy grain mount together with Geological Survey of Canada (GSC) natural monazite standards. The mount was polished to reveal grain centers and coated with 5.8–6.0 nm of Au (99.9999%). BSE images for monazite crystals were obtained at the GSC using a Cambridge Instruments S360 scanning electron microscope operating at 20 kV accelerating potential and using an electron beam current of 2–5 nA. In addition, kyanite and garnet mineral separates from DG38a were mounted, polished, and imaged using BSE. This approach provided rapid access to a greater number of porphyroblasts that might contain monazite inclusions relative to analysis of grains within individual thin sections. Despite lacking the textural information provided by analysis of a polished thin section, textural evidence for crystals concentrated in the grain mount could be indirectly furnished from thin section observations using a polarizing microscope.

Chemical maps of Y, Th, and U in selected monazite crystals from both grain mounts were made using a Cameca SX50 electron microprobe at the University of Massachusetts according to procedures outlined by Williams et al. (1999). High-resolution X-ray maps of Y, Th, and U were produced using a high current (240 nA), small step sizes (~0.5 μm), and rastering of the electron beam. Obtaining chemical maps of monazite prior to SHRIMP II analysis is unique to this study and proved to be very effective for elucidating age domains within the analyzed monazite.

Ion microprobe analysis of monazite grains was carried out using the SHRIMP II facility at the GSC in Ottawa, according to the methods outlined by Stern (1997), Stern and Sanborn (1998), and Stern and Berman (2000). Target locations for U–Th–Pb SHRIMP analysis on selected monazite grains were chosen using the images acquired from the techni-

ques described above. Targeted areas were sputtered using a mass-filtered O_2^- primary beam operating in Kohler illumination mode to effect even sputtering. All samples were analyzed using a single primary beam aperture setting, which yielded an approximate spot diameter of 22×31 μm. For monazite, the primary beam current was ~2–2.3 nA for both standards and unknowns. The operational mass resolution (1% peak height) over the course of the analysis was 5550–5700. Instrumental bias in the measured Pb/U and Pb/Th ratios was corrected by an empirically derived calibration of the linear relationships between $^{206}Pb^+/UO^+$ vs. UO_2^+/UO^+ and $^{208}Pb^+/ThO^+$ vs. UO_2^+/UO^+, respectively, determined on natural intermediate Th GSC monazite standard #3345 (mean Th wt.% = 7.3). Monazite standard #3345 is known from repeated BSE imaging to be relatively weakly zoned and from numerous ID-TIMS and SHRIMP analyses to be dominated by domains uniform in U and Th concentration. Nonetheless, uncertainties in the calculated U and Th abundances measured using the ion probe are likely no better than ±20% (see Stern and Berman, 2000). Isotopic ratios were corrected for common Pb using ^{204}Pb. However, for SHRIMP data, the ^{204}Pb correction can impart

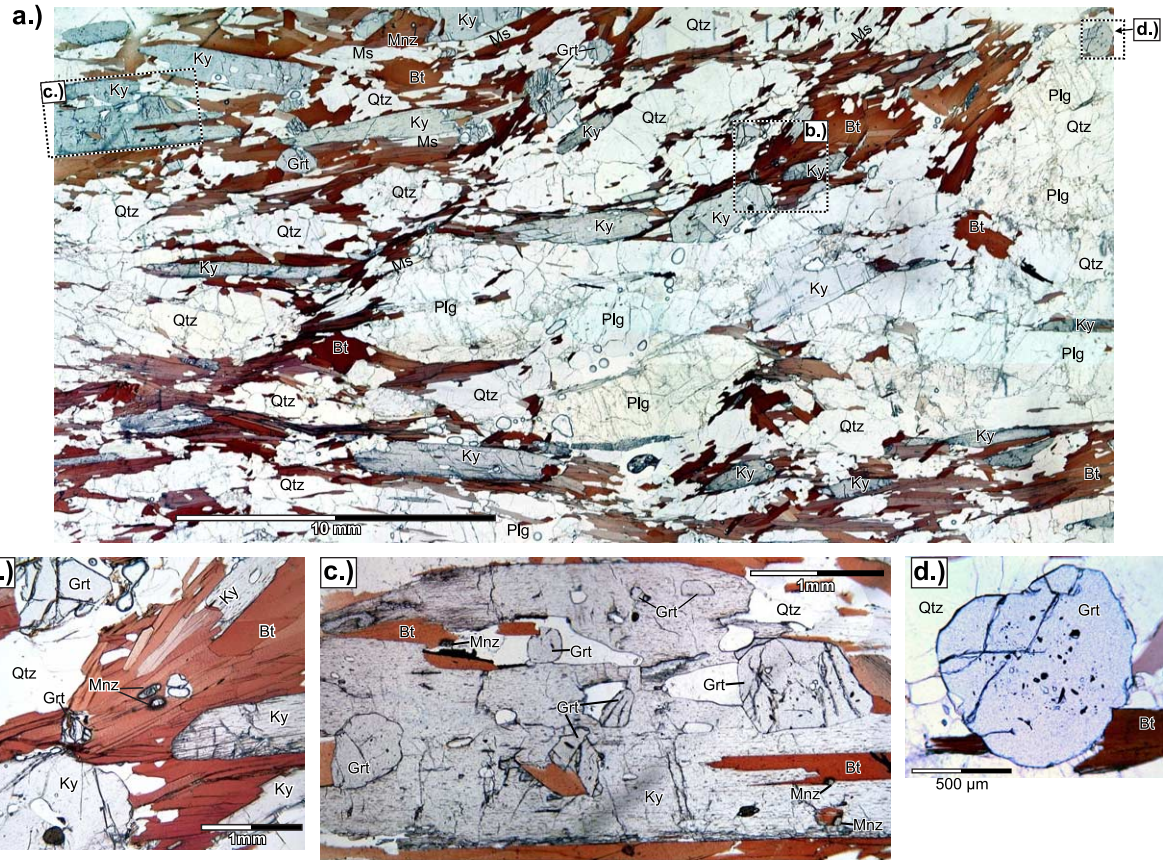

Fig. 2. (a) Photomicrograph of DG38a thin section, a muscovite–garnet–kyanite–biotite+melt pelitic schist. (b) Two monazite grains in the center of the photo align within the foliation of DG38a. Presumably, dating these monazite grains should provide upper age limits for the formation of the foliation in DG38a. Aside from the structural oversimplification, this interpretation is complicated due to the likelihood of multiple age domains within single crystals. (c) Closeup of upper left portion of thin section in (a), showing resorption features of kyanite and garnet, as well as the garnet inclusions within kyanite. Note that the garnet in the mid-right portion of the photo has inclusion trails within the core surrounded by an inclusion-free rim that appears to obtrude into the nearby kyanite. (d) Closeup of garnet from the upper right portion of the thin section shown in (a), displaying an inclusion-rich core surrounded by a relatively inclusion-free rim.

Table 1
U–Pb ID-TIMS analytical data for DG38a

Fraction[a]	Wt.[b] (μg)	U (ppm)	Pb*[c] (ppm)	$^{206}Pb/^{204}Pb$[d]	Pb[e] (pg)	^{208}Pb[f] (%)	$^{206}Pb/^{238}U$[g] (%)	$^{207}Pb/^{235}U$[g] (%)	$^{206}Pb/^{238}U$[h] (Ma)	$^{207}Pb/^{235}U$[h] (Ma)	Rho	$^{207}Pb/^{206}Pb$[g] (%)	$^{207}Pb/^{206}Pb$[h] (Ma)	Disc.[i] (%)
DG38a muscovite–garnet–kyanite–biotite pelitic schist														
M2>202	28	4280	194	2568	48	67.5	0.016239±0.56	0.10758±0.57	103.8±1.2	103.7±1.1	0.98	0.04805±0.10	101.6±4.9	−2.2
M3>202	25	4954	238	5874	26	63.5	0.019337±0.18	0.12956±0.19	123.5±0.4	123.7±1.1	0.95	0.04859±0.06	128.2±2.9	3.7
M4>202	20	5801	231	3913	30	63.4	0.016062±0.39	0.10627±0.40	102.7±0.8	102.5±0.8	0.98	0.04799±0.08	98.7±4.0	−4.1
M5>202	17	6710	288	5209	24	64.1	0.017032±0.29	0.11332±0.30	108.9±0.6	109.0±0.6	0.94	0.04826±0.10	111.8±4.8	2.6

[a] M2–M5 fraction code for single-grain monazite analysis; >202=grain diameter greater than 200 μm.
[b] Wt.=Weights, estimated from grain-size measurements; uncertainty is 2 μg.
[c] Radiogenic Pb.
[d] Measured ratio, corrected for spike and Pb fractionation of 0.09±0.03%/a.m.u.
[e] Total common Pb in analysis, corrected for spike and fractionation.
[f] Radiogenic ^{208}Pb, expressed as percentage of total radiogenic Pb.
[g] Corrected for Pb and U laboratory blank where 208/204:207/204:206/204=19.01:15.64:38.23:1, and common Pb (Stacey–Kramers model Pb composition equal to interpreted age of analysis); errors are one standard error of the mean in percent.
[h] Corrected for common Pb and laboratory blank; errors are two standard errors of the mean (2σ) in Ma.
[i] Disc.=Discordance in percent relative to the $^{207}Pb/^{206}Pb$ age=$100\times[1-(^{206}Pb/^{238}U$ age)/($^{207}Pb/^{206}Pb$ age)].

significant error on the calculated age due to extremely low ^{204}Pb counts (see Stern, 1997). The propagation of the statistical error associated with this has a large impact on the ^{207}Pb/^{235}U age because of low ^{207}Pb counts in Mesozoic or younger minerals. Furthermore, the lack of precision in some ^{207}Pb analyses may cause artificial disagreement between the calculated ^{207}Pb/^{235}U age and those based on other decay schemes. Thus, for monazite, the ^{208}Pb/^{232}Th chronometer is considered most accurate because it includes the highest Pb counts and is apparently unaffected by isotopic disequilibrium (i.e., unsupported ^{206}Pb). For this reason, in the following sections and figures, quoted ages rely on the ^{208}Pb/^{232}Th chronometer even though in some cases it is apparently less precise than the Pb/U chronometers. Errors assigned to SHRIMP U–Th–Pb ages were determined using numerical propagation of all known sources of error as outlined by Stern (1997), Stern and Sanborn (1998), and Stern and Berman (2000).

4. Results

Monazite U–Th–Pb data for DG38a, a medium-grade metapelitic sample (Fig. 2) from the northern Selkirk Mountains, are presented below (all age errors reported at two standard errors, 2σ). The ID-TIMS data are presented in Table 1 and the U–Pb concordia plot of Fig. 3a. The SHRIMP data are presented in Table 2 and the U–Pb concordia plots of Figs. 3b–7, which also include the BSE and Y, Th, and U chemical map images. For each Y map, the approximate Y concentration in parts per million (ppm) for each pixel was calculated using the AgeMap program as modified by Goncalves et al. (in press, American Mineralogist, 2004). This pro-

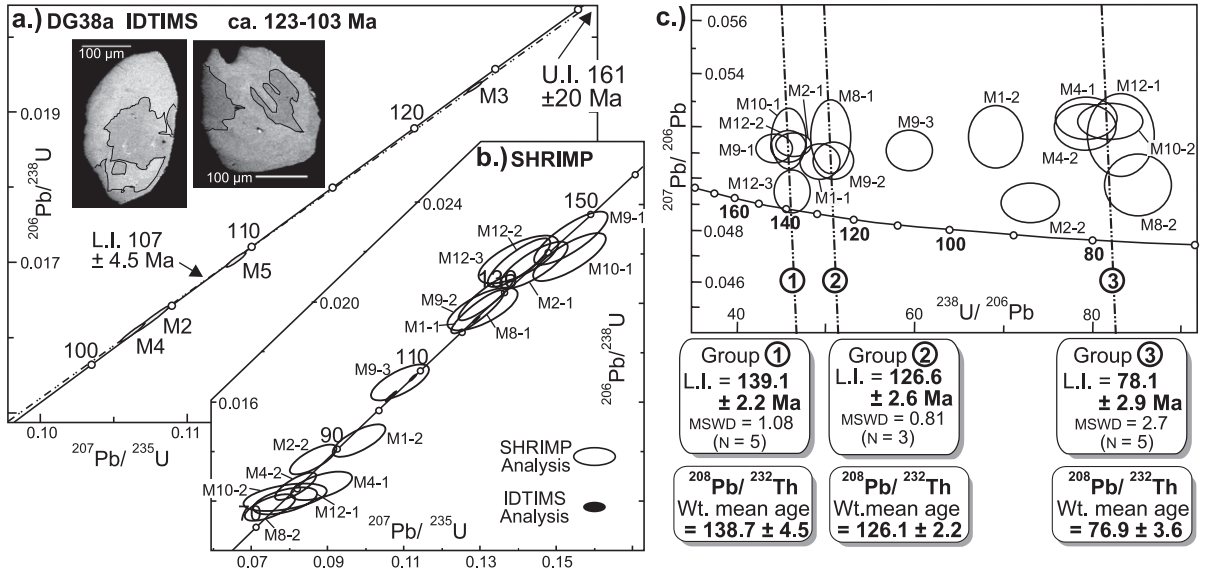

Fig. 3. (a) U–Pb concordia plot for DG38a illustrating the spread of ID-TIMS data from single crystal monazite fractions in close proximity to the concordia curve. Inset BSE images of other representative monazite grains from DG38a reveal chemical zoning that may represent multiple age domains within single crystals. The upper and lower intercepts (U.I. and L.I., respectively) of the discordia line are considered to be geologically meaningless due to the likelihood of multiple age domains within single crystals and the presence of unsupported ^{206}Pb. (b) U–Pb concordia plot illustrating the range of SHRIMP spot ages for monazite of DG38a. Notation for each ellipse represents the monazite grain followed by the spot number, i.e., M1-1 equals Mnz1, spot 1. (c) A Tera-Wasserburg (T-W) plot highlights the various age domains within monazite grains of DG38a. In the T-W plot, the ^{207}Pb/^{206}Pb ratio uncorrected for common Pb is plotted against uncorrected ^{238}U/^{206}Pb. Ages for each group of data are provided by the intercept of a linear regression through the data with the concordia curve (N=5, represents number of data points used in each regression). The weighted (Wt.) mean of the ^{208}Pb/^{232}Th ages for each group is included below the T-W plot for comparison;

Table 2
SHRIMP U–Th–Pb analytical data for sample DG38a

Spots[a]	U (ppm)	Th (ppm)	Th/U	Pb*[b] (ppm)	^{204}Pb (ppb)	^{206}Pb/^{204}Pb	^{208}Pb/^{232}Th[c]	^{206}Pb/^{238}U[c]	^{207}Pb/^{235}U[c]	^{207}Pb/^{206}Pb[c]	^{208}Pb/^{232}Th[d] (Ma)	^{206}Pb/^{238}U[d] (Ma)	^{207}Pb/^{235}U[d] (Ma)	Rho
DG38a muscovite–garnet–kyanite–biotite pelitic schist														
M1.1	16972	116552	6.87	953	67	4403	0.0063±0.0001	0.0202±0.0004	0.1318±0.0029	0.0474±0.0005	127.1±3.8	128.8±4.6	125.7±5.2	0.88
M1.2	17886	100243	5.60	629	33	6661	0.0045±0.0001	0.0144±0.0003	0.0983±0.0029	0.0495±0.0010	91.2±2.8	92.3±3.4	95.2±5.2	0.71
M2.1	15792	112385	7.12	965	52	5651	0.0067±0.0001	0.0215±0.0004	0.1443±0.0036	0.0487±0.0007	134.7±4.2	137.0±5.0	136.9±6.4	0.80
M2.2	17623	110604	6.28	627	46	4525	0.0043±0.0001	0.0136±0.0003	0.0862±0.0025	0.0458±0.0009	85.7±2.6	87.4±3.2	84.0±4.6	0.72
M4.1	15819	132005	8.34	635	16	10848	0.0039±0.0001	0.0126±0.0002	0.0885±0.0033	0.0510±0.0015	79.3±2.4	80.6±2.8	86.1±6.0	0.59
M4.2	15190	102313	6.74	522	54	3040	0.0039±0.0001	0.0126±0.0002	0.0818±0.0022	0.0472±0.0008	78.9±2.4	80.5±2.8	79.8±4.0	0.76
M8.1	13545	74316	5.49	647	56	4110	0.0062±0.0001	0.0197±0.0004	0.1307±0.0038	0.0481±0.0010	125.7±3.8	125.8±4.4	124.8±6.8	0.71
M8.2	22064	97160	4.40	539	50	4410	0.0036±0.0001	0.0117±0.0002	0.0750±0.0027	0.0464±0.0013	72.6±2.2	75.0±2.6	73.4±5.0	0.61
M9.1	15404	126280	8.20	1107	35	8590	0.0072±0.0001	0.0226±0.0004	0.1540±0.0039	0.0495±0.0007	144.4±4.4	143.9±5.4	145.4±7.0	0.82
M9.2	27170	106203	3.91	1058	87	5256	0.0062±0.0001	0.0196±0.0004	0.1294±0.0028	0.0479±0.0005	125.6±3.8	125.0±4.4	123.6±5.0	0.89
M9.3	17890	98687	5.52	731	69	3730	0.0053±0.0001	0.0168±0.0003	0.1090±0.0031	0.0472±0.0010	107.4±3.2	107.1±3.8	105.1±4.8	0.72
M10.1	13247	95330	7.20	843	9	27933	0.0070±0.0001	0.0218±0.0004	0.1535±0.0039	0.0511±0.0008	140.3±4.2	139.1±5.0	145.0±7.0	0.78
M10.2	17375	107257	6.17	553	63	2902	0.0039±0.0001	0.0121±0.0002	0.0789±0.0045	0.0472±0.0024	78.3±2.4	77.7±2.8	77.1±8.4	0.44
M12.1	11988	96584	8.06	448	33	3781	0.0038±0.0001	0.0120±0.0002	0.0789±0.0034	0.0478±0.0017	75.9±2.4	76.7±2.8	77.1±6.4	0.54
M12.2	16097	101479	6.30	922	91	3298	0.0069±0.0001	0.0217±0.0004	0.1402±0.0043	0.0468±0.0011	138.1±4.2	138.5±5.0	133.2±7.6	0.68
M12.3	22341	109505	4.90	1082	67	6222	0.0068±0.0001	0.0216±0.0004	0.1402±0.0033	0.0472±0.0006	136.9±4.2	137.6±4.8	133.2±6.0	0.82

[a] Spots are denoted as follows: M1.1=monazite and spot number.
[b] Radiogenic Pb.
[c] Corrected for common Pb according to procedure outlined by Stern and Berman (2000); uncertainties are reported at 1σ and are calculated by numerical propagation of all known sources of error.
[d] Age errors reported at 2σ in Ma.

gram was used to estimate the approximate Y concentration for each SHRIMP spot (Table 3), as well as provide plots of Y concentration for selected profiles across each grain (Figs. 4–8). In Fig. 3b, the SHRIMP data are also plotted in a Tera-Wasserburg diagram (Tera and Wasserburg, 1972), in which the $^{207}Pb/^{206}Pb$ ratio uncorrected for common Pb is plotted against the uncorrected $^{238}U/^{206}Pb$ ratio. Linear regressions were calculated for data that clustered in distinguishable groups. The age for a particular group was determined using the lower intercept of the regression line with the concordia curve. The upper end of the chord was anchored at the common $^{207}Pb/^{206}Pb$ composition representing the approximate age of each group using Stacey and Kramers (1975) model growth curves.[1] Ages derived from the lower intercepts of the regressions avoid the potentially large uncertainty imposed by the ^{204}Pb correction for common Pb. The data in the Tera-Wasserburg plot also provide a visual estimate of the common Pb component (see Compston et al., 1992). Although the calculated ages may be affected by variable amounts of unsupported ^{206}Pb, they appear to have good agreement with the $^{208}Pb/^{232}Th$ ages (Fig. 3c). The Tera-Wasserburg plot also helps to highlight the age domains within DG38a, as well as within individual monazite crystals.

Table 3
Yttrium concentration for SHRIMP spots

	Spot#	Y (ppm)[a]	$^{208}Pb/^{232}Th$ (Ma)	Age group[b]
Mnz1	M1-1	~5120	127.1±1.9	2
	M1-2	~15800	91.2±1.4	–
Mnz2	M2-1	~6480	134.7±2.1	1
	M2-2	~18450	85.7±1.3	–
Mnz4	M4-1	~21620	79.3±1.2	3
	M4-2	~23500	78.9±1.2	3
Mnz8	M8-1	~6400	125.7±1.9	2
	M8-2	~21080	72.6±1.1	3
Mnz9	M9-1	~2200	144.4±2.2	1
	M9-2	~12490	125.6±1.9	2
	M9-3	~22500	107.4±1.6	–
Mnz10	M10-1	~4275	140.3±2.1	1
	M10-2	~22700	78.3±1.2	3
Mnz12	M12-1	~21150	75.9±1.2	3
	M12-2	~3180	138.1±2.1	1
	M12-3	~10500	136.9±2.1	1

[a] Average Y ppm calculated for area covered by the SHRIMP spot determined using the AgeMap program as modified by Goncalves et al. (in press, American Mineralogist).

[b] Age group to which SHRIMP spot age is assigned (see Fig. 3b); spots that may have overlapped more than one domain are not assigned to an age group (–).

4.1. DG38a—muscovite–garnet–kyanite–biotite pelitic schist

Sample DG38a is a foliated migmatitic muscovite–garnet–kyanite–biotite pelitic schist (minerals listed by increasing modal abundance), with monazite, apatite, and zircon as the main accessory phases. DG38a is interlayered with a biotite-rich psammite; layers are ~50 cm to 1 m thick. Approximately 20–30% of the observable outcrop contains foliated leucosome lenses composed primarily of plagioclase, quartz, and cross-cutting muscovite. All kyanite and most biotite are aligned within a shallow southwest dipping foliation that is pervasive throughout the area (Fig. 2a). Many monazite grains identified using a polarizing microscope appear to be aligned parallel to the foliation (Fig. 2b). Shear bands related to south-west-directed late normal faulting are superimposed on the entire assemblage (Fig. 2a).

Both garnet and kyanite are subhedral and display significantly resorbed grain boundaries, replaced by biotite, and to a lesser extent quartz and plagioclase (i.e., melt) with some minor muscovite (Fig. 2a–c). Most biotite and muscovite are euhedral, and are interpreted to be part of the latest stable assemblage with quartz and plagioclase (Fig. 2c), perhaps products of melt crystallization. Although not observed in this sample, retrograde chlorite is found nearby (<500 m) as another late replacement of garnet. Some garnet grains appear to be included within large kyanite laths, while others appear to have overgrown kyanite (Fig. 2c). These observations suggest there may have been more than one episode of garnet growth, however, based on this two-dimensional slice it is difficult to definitively interpret whether kyanite overgrew garnet or garnet overgrew kyanite, or both. Nonetheless, some of the garnet porphyroblasts have cores with inclusions of quartz, opaques, and less commonly monazite surrounded by inclusion-free, homogeneous rims (Fig. 2d), which

[1] It was not necessary to know the exact $^{207}Pb/^{206}Pb$ ages when calculating the Stacey-Kramer common Pb composition because there is <1% variation in the common $^{207}Pb/^{206}Pb$ ratio for Jurassic-Cretaceous ages.

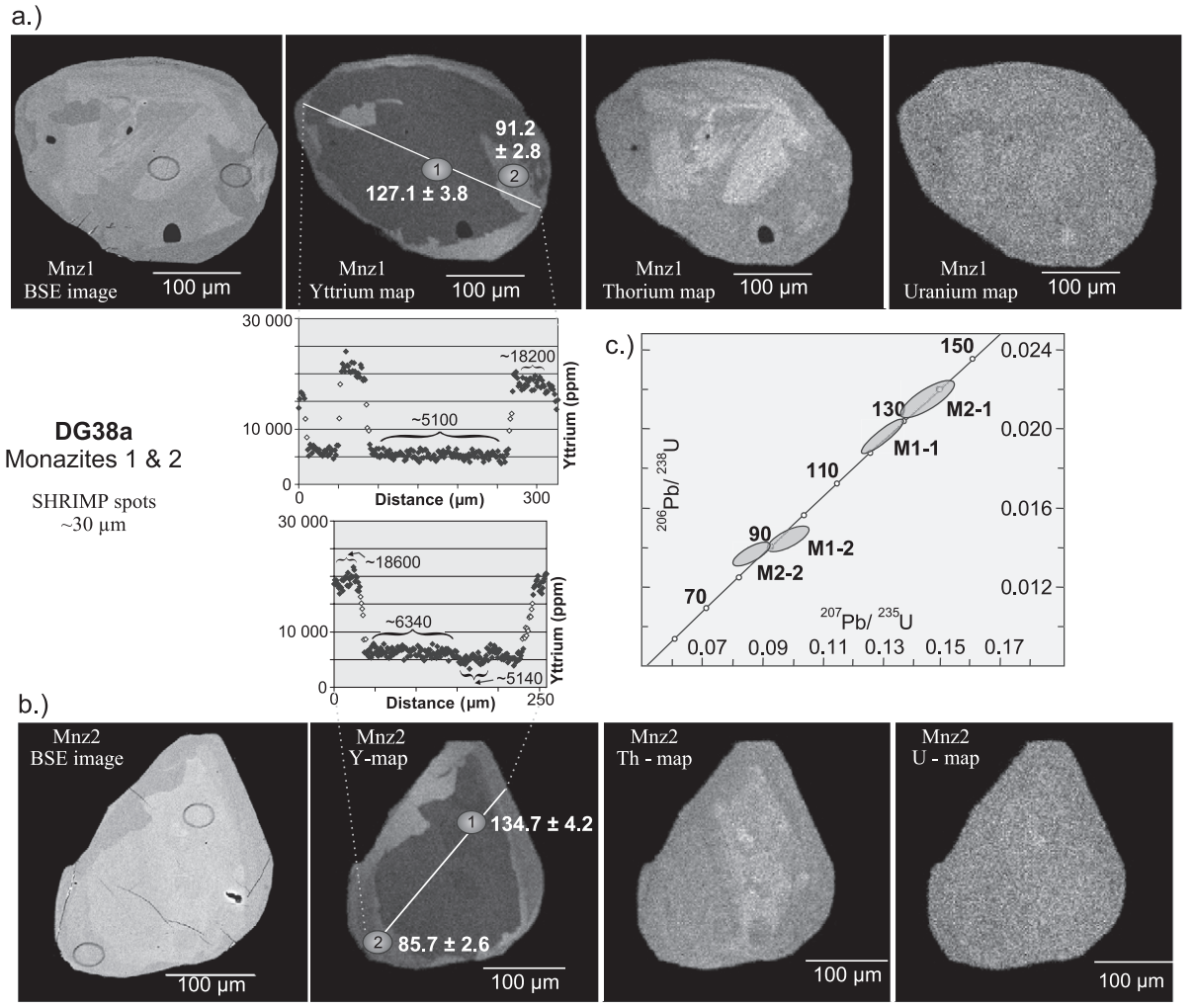

Fig. 4. (a) and (b) BSE images, Y, Th, and U maps, respectively, of monazite 1 and 2 (Mnz1 and Mnz2) that were analyzed by the SHRIMP. For the chemical maps, brighter domains correspond to higher elemental concentrations. The Y domains were used as a guide to target the SHRIMP analyses. The locations of the SHRIMP spots, and their numbers, are shown within the BSE and Y images. The $^{208}Pb/^{232}Th$ ages for each spot are also provided in the Y maps (see Table 2). Each Y map is also accompanied by a profile of Y concentration (ppm) across the grain. Each diamond in the profile represents the average Y ppm of 4 pixels. Note: white diamonds represent averages calculated across the boundary of two domains. Within the Y plots, brackets with a number above provide the average Y ppm for a given domain. (c) U–Pb concordia plot that includes the spot analyses for each monazite domain analyzed.

further suggests more than one episode of garnet growth.

An effort was made to sample mainly the restitic portion of DG38a. However, the pervasiveness of the melt made this difficult, and it is likely that mineral separates included monazite from both the pelitic and leucosome portions of the outcrop. The ID-TIMS analysis of single-grain monazite fractions plot in close proximity to the concordia curve between ca. 123 to 103 Ma (Fig. 3a). Fractions M2 and M4 are reversely discordant and plot just above the concordia curve (−2.3% and −4.1% discordant, respectively; negative values assigned to reverse discordance). Conversely, M5 and M3 are normally discordant and plot just below the concordia curve (2.6% and 3.7% discordant, respectively). A linear regression through the data produces a lower intercept (L.I.) of 107±4.5 Ma and an upper intercept (U.I.) of 161±20

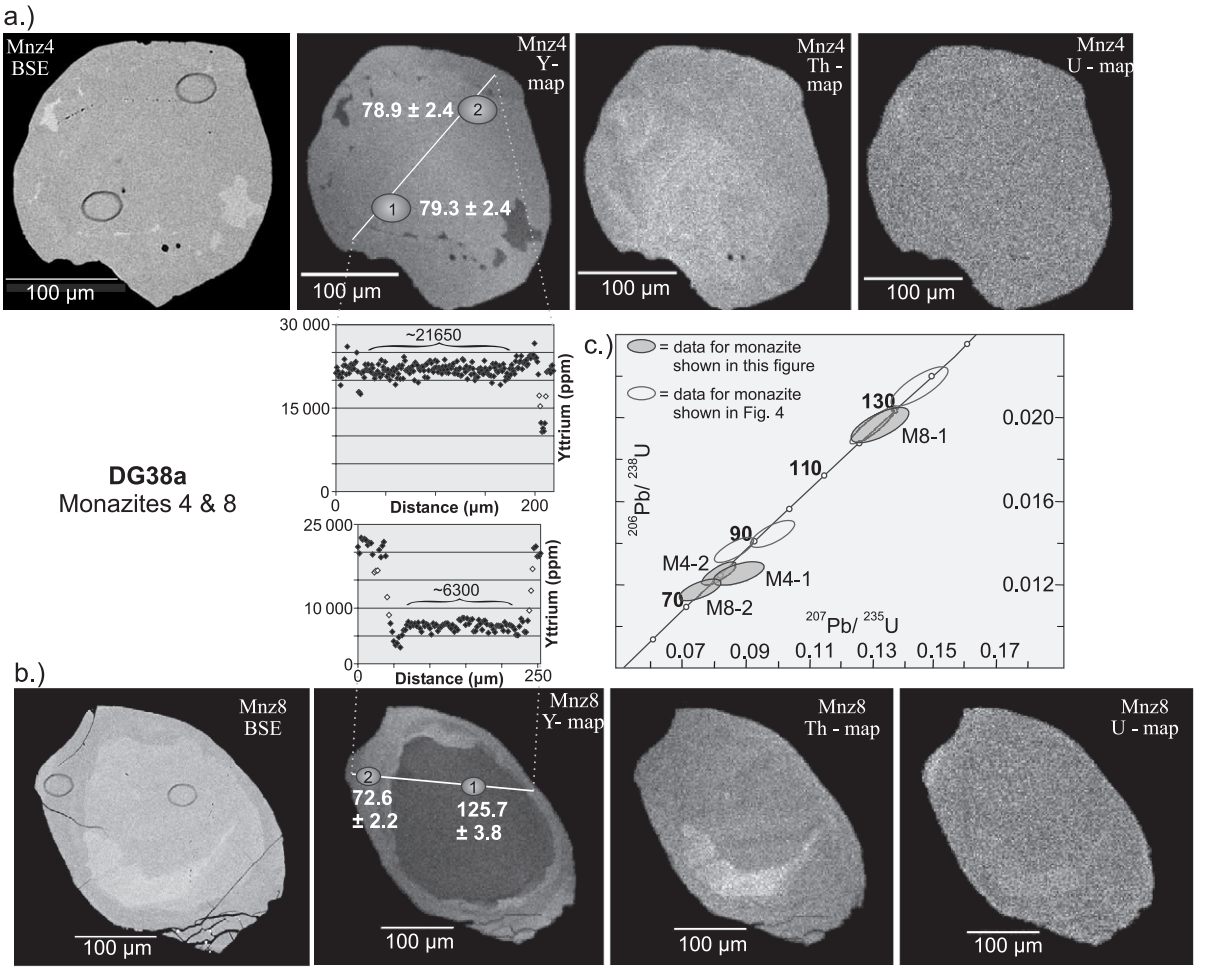

Fig. 5. This figure, Figs. 6, and 7 have a similar layout as Fig. 4. (a) and (b) BSE images, Y, Th, and U maps of Mnz4 and Mnz8, respectively. (c) U–Pb concordia plot of the SHRIMP data; shaded ellipses represent data for Mnz4 and Mnz8 (i.e., current figure), whereas open ellipses are the data presented in the previous figure (i.e., Mnz1 and Mnz2).

Ma. The intercept ages agree well with other age constraints in the region, but are considered spurious for the following reasons: (1) The L.I. is older than the youngest monazite fractions, M4 and M2, a result of a linear regression through reversely discordant data. (2) The discordia chord plots very close to the concordia curve. This imparts substantial error on the upper intercept age because of the low angle intersection of the chord with the concordia curve. (3) BSE images of monazite grains for DG38a show complex and irregular chemical domains, possibly indicative of multiple age domains within single monazite crystals (inset Fig. 3a). Thus, the likelihood of bulk mixing of multiple age domains with or without varying degrees of unsupported ^{206}Pb makes it difficult or impossible to correctly interpret the ID-TIMS data using linear regression techniques.

In situ SHRIMP analysis has confirmed the existence of multiple intracrystal age domains. Prior to the ion probe analysis, BSE imaging and X-ray elemental mapping for Y, Th, and U revealed complex zoning in many of the monazite grains. The Y maps generally provided the best indication of growth and/or recrystallization domains, and were critical for targeting SHRIMP analysis because these relation-

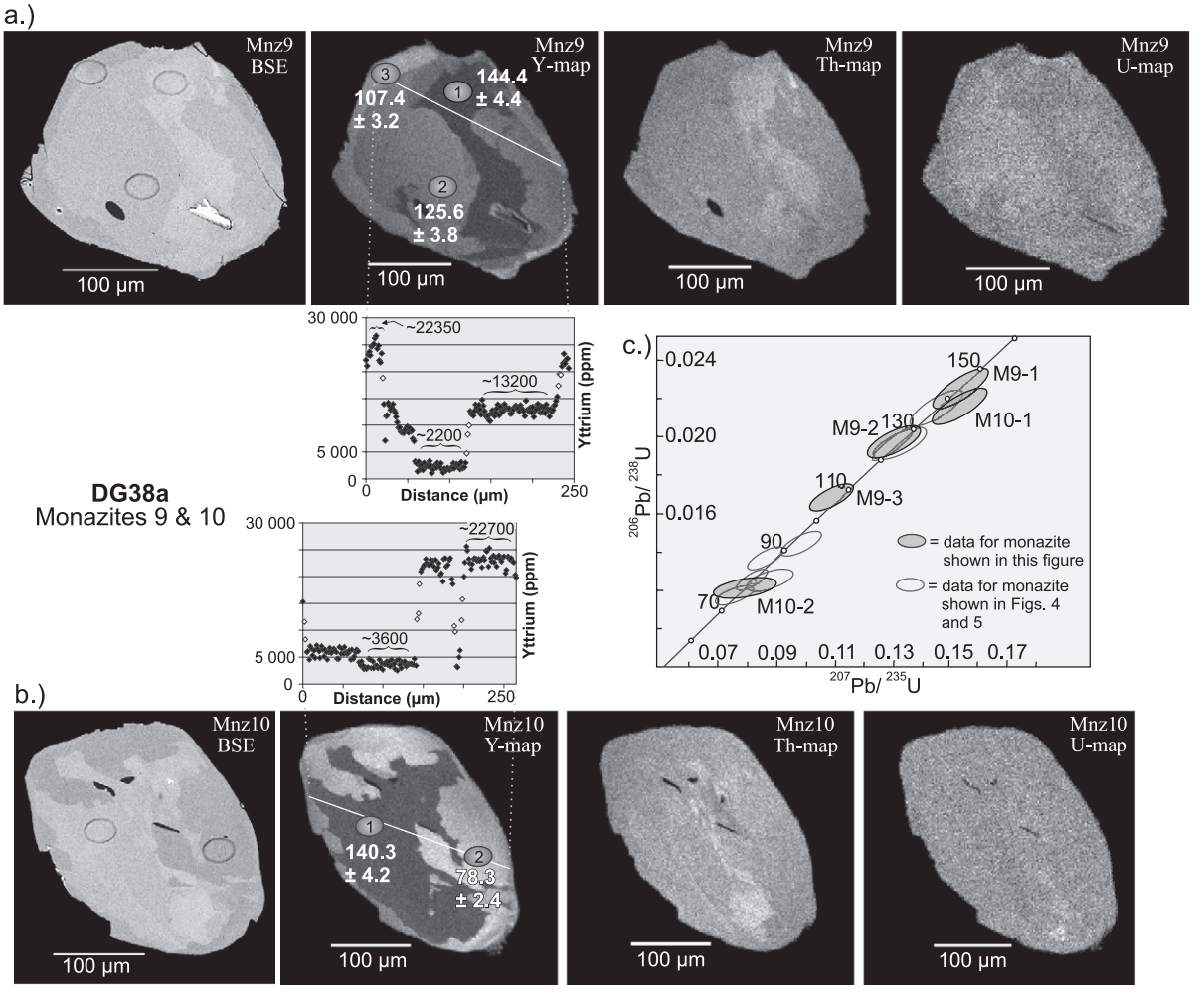

Fig. 6. (a) and (b) BSE images, Y, Th, and U maps of Mnz9 and Mnz10, respectively. (c) U–Pb concordia plot of SHRIMP data for current and previous figures.

ships were not always clear in BSE, U, and Th images.

At least three, and possibly five, ages of monazite crystallization were identified when the Y images were used to target the SHRIMP analysis (Figs. 4–7). The oldest ages have a weighted mean $^{208}Pb/^{232}Th$ age of 138.7±4.5 Ma that includes five SHRIMP spots on four monazite grains (see Fig. 3b and c). These ages correspond to the lowest Y domains (~2200 to 10500 ppm, Table 3), located in the core portion of the analyzed monazite (Mnz2, 9, and 10 of Figs. 4b and 6, respectively). There is one exception, Mnz12 has a younger (75.9±2.4 Ma), high Y zone (~21150 ppm) in the core partly surrounded by the older, lowest Y domain (~3180 ppm; Fig. 7a). However, the high Y 'core' has the same concentration as the high Y rim of this monazite, thus, both are interpreted to be part of the same domain. The central high Y portion likely represents a lobe of the younger rim that extended down (*z*) into the plane (*x*–*y*) of the image.

The second oldest domain within the monazite of DG38a has a weighted mean $^{208}Pb/^{232}Th$ age of 126.1±2.2 Ma based on three spots (M1-1, M8-1, M9-2; Fig. 3c) on three monazite grains (Figs. 4–6). This corresponds with the zones that typically have

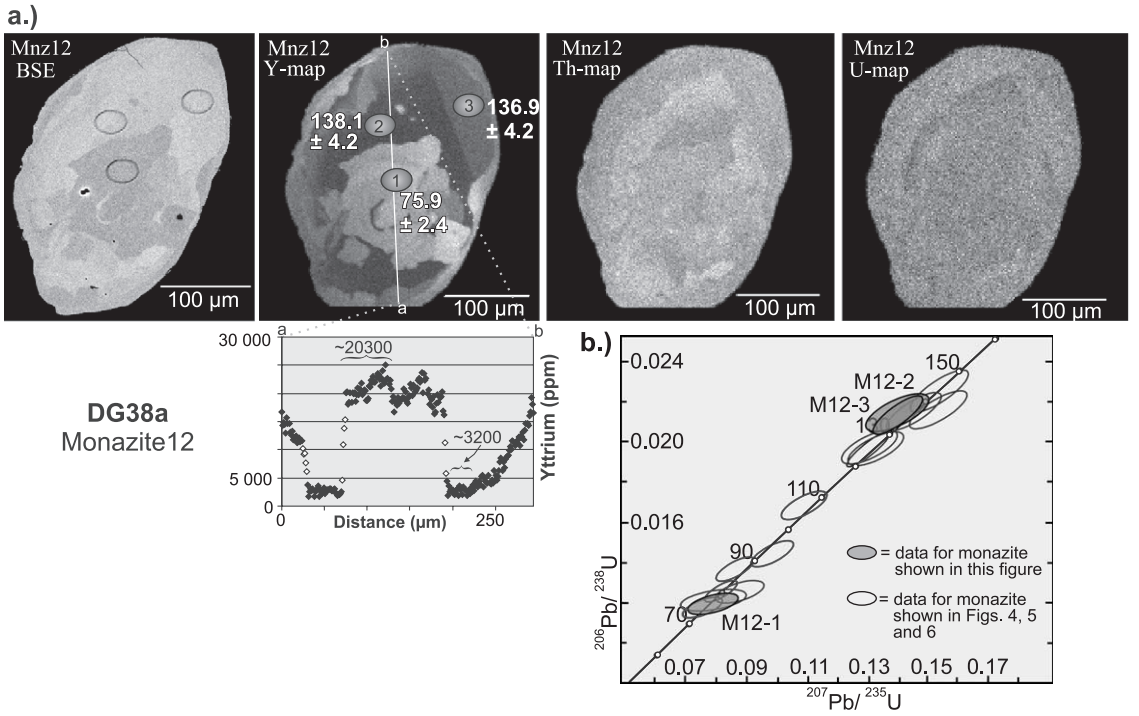

Fig. 7. (a) BSE images, Y, Th, and U maps of Mnz12. (b) U–Pb concordia plot of SHRIMP data for monazite presented in this figure and in Figs. 3–6.

the second lowest Y concentration (~5120–12490 ppm; Table 3) that are distinct from the older, lowest Y domains described above. For instance, in Mnz9, there is a sharp, truncated boundary between the younger (125.6±3.8 Ma) intermediate Y domain, and the older (144.4±4.4 Ma) lower Y core that was significantly resorbed. The SHRIMP spots are clearly situated within their respective Y zones (Fig. 6a), leaving little doubt that these are robust ages for separate growth domains.

The youngest domain in all the monazite analyzed is associated with discordant, high Y rims (~21 080–22 700 ppm; Table 3), except for Mnz4 (Fig. 5), which is almost entirely composed of this high Y domain. The limited preservation of small, isolated patches of low Y concentration in Mnz4 suggest that resorption and/or recrystallization of this domain was nearly complete. The high Y domains appear to range in age from 107.4±3.2 to 72.6±2.2 Ma (Figs. 4–7; Tables 2 and 3). However, the weighted mean $^{208}Pb/^{232}Th$ age of 76.9±3.6 Ma for five spots on four monazite grains is considered to be the best approximation for this domain, i.e., Group 3 in Fig. 3c. The older ages are likely the result of slight overlap into older, adjacent age domains. This is clearly the case for spot 3 of Mnz9, which is 107.4±3.2 Ma (Fig. 6a) and possibly for spot 2 of Mnz1, which is 91.2±2.8 Ma (Fig. 4a). Spot 2 of Mnz2 (85.7±2.6 Ma) overlaps a faint, slightly lower Y domain within the rim that could account for its older age (Fig. 4b).

The results demonstrate that the Y concentrations for the domains assigned to a specific "Group" are not uniform, and of the three age groups described above, SHRIMP spots assigned to Groups 1 and 2 appear to have substantial overlap between their Y ppm values (Table 3). The proximity of the analyzed monazite to sites of garnet breakdown or formation and thus the relative amount of Y available to incorporate may account for the observed variance. Nevertheless, a general pattern emerges; that is, the oldest SHRIMP spots assigned to Group 1 are located within the lowest Y ppm domain for those monazite grains, whereas analyses belonging to Group 2, especially for Mnz9, have a slightly higher Y content. It is

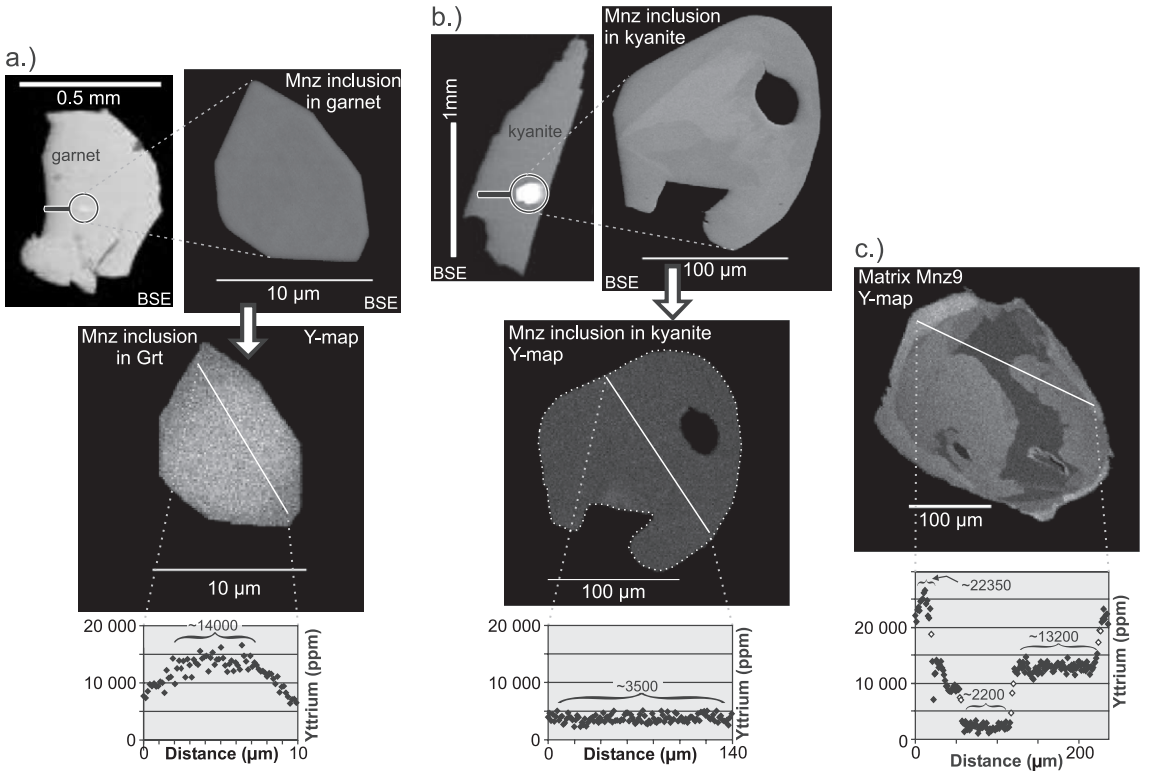

Fig. 8. Comparison of Y maps and Y ppm for monazite inclusions in garnet and kyanite with matrix monazite (i.e., Mnz9, see below). (a) Monazite inclusion found in the core of a garnet displays a fairly uniform Y concentration; ~14 000 ppm Y in the core progressively decreases toward the rim. Domains of similar Y concentration were not found in the matrix monazite that were analyzed (see Table 3), suggesting that preservation of monazite grains with a similar Y content likely occur only as inclusions armored by garnet. (b) A monazite included within kyanite also has a uniform Y concentration (~3500 ppm), which matches very closely with the Y concentration in the oldest parts of the matrix monazite (see Table 3). (c) Y map of Mnz9. This is considered to be a matrix monazite due to the multiple, irregularly shaped zoning patterns and relatively large size (~320×240 µm) compared to the monazite inclusions within garnet (a) and kyanite (b).

unequivocal that the youngest ages assigned to Group 3 are within the highest Y domains of all analyzed monazite, with approximately twice the Y content (ppm) vs. Group 1 or 2 (Table 3).

5. Discussion

5.1. Why do the Y maps provide the best indication of age domains?

In this study, the Y maps consistently provide the best independent proxy for age domains within the metamorphic monazite. Although many of the zones revealed within the BSE images closely approximates those in the Y maps, some BSE images appear more texturally complex and/or lack the definition provided by the Y maps (Figs. 4–7). Other studies have documented the lack of correlation between BSE images and age domains determined using in situ techniques (e.g., SHRIMP in Rubatto et al., 2001; EMP in Cocherie et al., 1998). The above observations may be attributed to the process involved in the generation of BSE images, where the production of backscattered electrons varies directly with atomic number; in general, higher atomic number elements appear brighter than lower atomic number elements. Discrimination of "chemical domains" by BSE imaging of minerals such as monazite arises from the differences in average atomic number within the crystal (cf. Stern and Sanborn, 1998). Since monazite typically contains several thousand ppm Th with a

high atomic number (Z=90), the zoning in BSE images should strongly reflect the Th distribution. However, the zoning may also be significantly influenced by the distribution of other elements such as U (Z=92; 100s to 1000s ppm) and possibly Ce (Z=58) and La (Z=57). Thus, the domains revealed in BSE imaging necessarily represent a composite image of superimposed chemical zones of more than one element, which is more visually complicated and less discrete compared to those found in an image generated from the analysis specifically for Y.

The zones and boundaries observed in the Th and U images tend to have less definition or were absent when compared to the sharp zoning produced by the Y maps (Figs. 4–7). This is primarily an analytical artifact related to the detector collection efficiency for X-rays of Th and U vs. those of Y (Goldstein et al., 1981). The quantum efficiency for detecting X-rays with a wavelength (λ) close to 4 Å (i.e., U=3.910 Å, Th=4.138 Å, as determined by Bearden, 1964) drops sharply to ~40% efficiency compared to X-rays with λ of 6.5 Å (Y=6.449 Å) that have ~80% detection efficiency. This accounts for the lack of resolution in the Th and U maps when compared to the Y maps in this study, but not for the lack of correlation between age domains and chemical zones in the Th and U maps. For instance, in Mnz2, 8, 9, and 10 (Figs. 4–6), the age domains identified using the Y maps could not be similarly correlated with zones in the U and Th maps. Williams et al. (1999) also demonstrated an inconsistent relationship between age domains and complex Th and U zoning within metamorphic monazite.

The cation sites preferentially occupied by Th and U vs. Y may account for their apparent noncorrelative nature regarding their distribution within a monazite crystal, and their correspondence, or lack thereof, with age domains (e.g., this study; Williams et al., 1999). However, this is still poorly understood. In monazite, all three elements occupy ninefold coordination sites (e.g., Yunxiang et al., 1995), are relatively abundant (1000s ppm to many %, e.g., Bea, 1996; Zhu and O'Nions, 1999a; Pyle et al., 2001), and have similar ionic radii (U=1.05 Å, Th=1.09 Å, Y=1.08 Å; Shannon, 1976). However, the difference in valence between Y^{3+} and U^{4+} and Th^{4+} does have an influence on both the lattice sites and the stoichiometry of coupled substitutions that accommodate the incorporation or removal of these elements during recrystallization processes (e.g., Bingen et al., 1996; Poitrasson et al., 1996, 2000). Another important and related factor is the influence other major and accessory minerals have on the availability of these elements during monazite production. Unfortunately, the influence of other minerals on the availability of Th (e.g., allanite, thorite, thorianite) and U (e.g., zircon, uraninite, epidote) for incorporation into metamorphic monazite is not well understood, especially for samples metamorphosed at medium to high grade. Conversely, a growing body of evidence strongly suggests that garnet exerts considerable control over the Y budget during metamorphism because it is a major Y sink (e.g., Bea and Montero, 1999; Foster et al., 2000, 2002; Pyle et al., 2001; Pyle and Spear, 2003). Consequently, reactions involving the production and consumption of monazite are sensitive to this, and are reflected internally in preserved Y zones.

5.2. Constraining the age of metamorphic reactions involving monazite

Using Gibbs method modeling, Pyle and Spear (2003) proposed a series of metamorphic reactions in which garnet, xenotime, and monazite share an intricate reaction coupling due to the high compatibility of Y in all three phases. Based on the clear relationship between Y and domains of growth-recrystallization in the monazite of DG38a, a tentative correlation is made with the reactions put forward by Pyle and Spear. Please note that the reactions proposed below are speculative, put forward as a testable model, and to demonstrate the potential of integrating in situ analyses with thermodynamic modeling. Also, the assemblage examined by Pyle and Spear was metamorphosed at lower pressures (≤4 kbar) than DG38a (~6–8 kbar); the reactions below, and summarized in Fig. 9, reflect this pressure difference.

Additional insight is provided by the textures in thin section, and by comparing the Y domains of the monazite analyzed by SHRIMP with those in monazite included in garnet and kyanite. In Fig. 8, the Y concentrations for monazite included within kyanite and garnet are uniform and mostly homogeneous, presumably because they were shielded from subse-

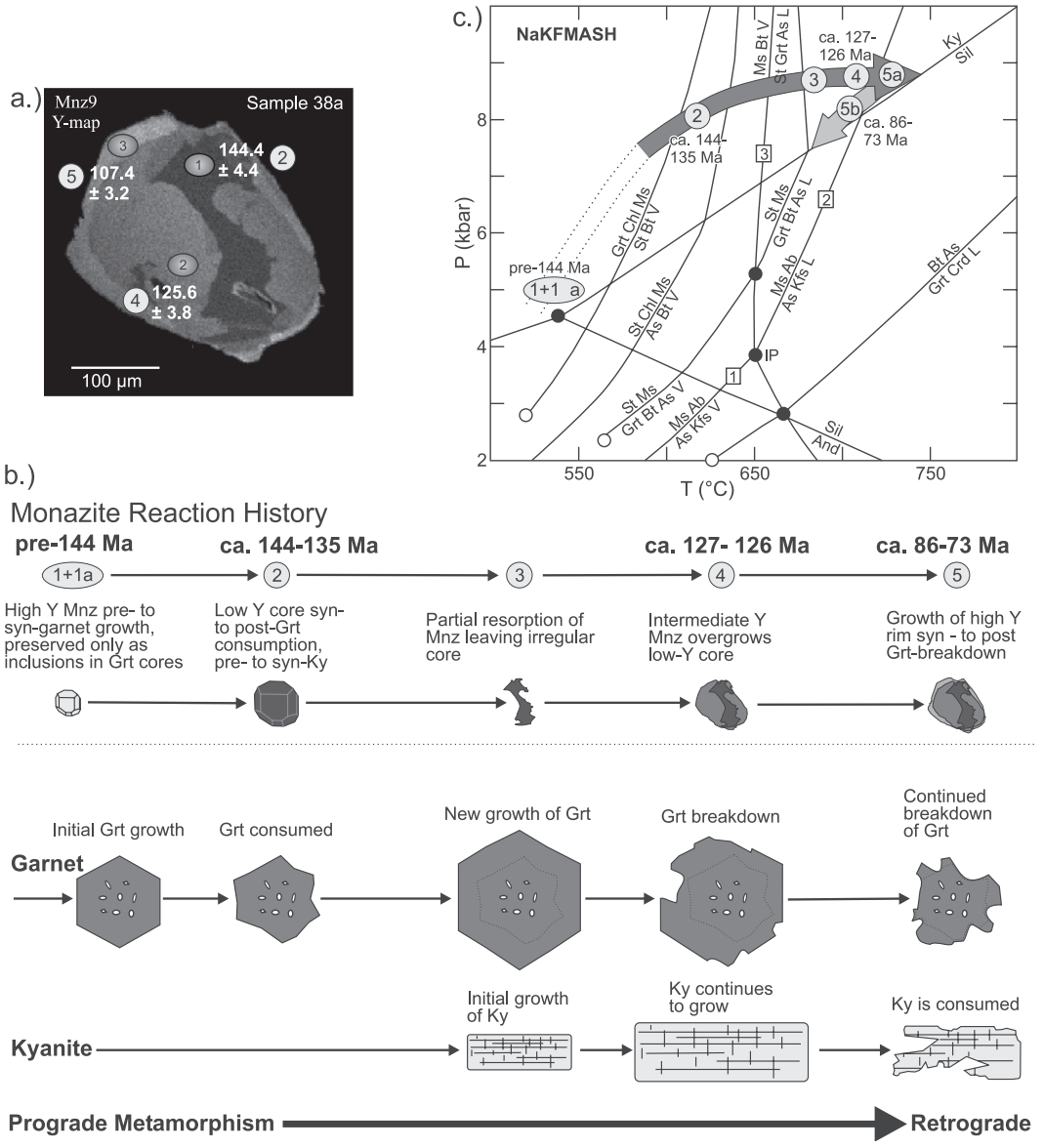

Fig. 9. (a) Y map for Mnz9 with SHRIMP spot locations and associated $^{208}Pb/^{232}Th$ ages. Note that spot 3 (i.e., 107.4±3.2 Ma) slightly overlaps the adjacent intermediate Y domain. Based on the other monazite analyses, the actual age for the high Y rim is interpreted to be ca. 86–73 Ma. The light grey numbered circles beside the ages correspond to metamorphic reactions discussed in text, as summarized in (b) and placed within the petrogenetic grid of (c). (b) Schematic representation of metamorphic history interpreted for monazite, garnet, and kyanite of DG38a. (c) Pressure–temperature–time path proposed for DG38a with the notation for each of the metamorphic reactions and their approximate timing constraints. The dark grey arrow represents the last part of the prograde path, based on the textures observed in thin section and the chemical maps, as well as the geothermobarometric constraints provided by the previous studies of Leatherbarrow (1981) and Ghent et al. (1979, 1982, 1983). The light grey arrow corresponds to the beginning of the retrograde path. The dotted portion of the *P–T–t* path represents the pre-144 Ma part of the prograde path for which there are no timing constraints and little or no metamorphic data. NaKFMASH petrogenetic grid is from Spear et al. (1999). Numbered squares correspond to melting reactions associated with univariant curves assigned by Spear et al. to the NaKFMASH grid; the intersection of these curves define invariant point IP1″. As=aluminosilicate; L=liquid; V=vapor.

quent metamorphic reactions. Conversely, monazite crystals in grain mount analyzed by the SHRIMP are interpreted as matrix monazite. They have multiple, irregularly shaped chemical domains, and are ≫100 μm in diameter, thought to be the result of unrestricted participation of these grains in the metamorphic reactions experienced by DG38a (cf. Foster et al., 2000; Pyle and Spear, 2003).

The monazite included within the garnet of Fig. 8a has a relatively high Y concentration (~14 000 ppm) that decreases progressively toward the rim. This value does not fall in the range of Y values within the matrix monazite (Table 3; Figs. 4–8). Also, the restricted grain size (<15 μm) of this monazite inclusion is characteristic of monazite that grew early in the prograde metamorphism of a pelitic assemblage (see Rubatto et al., 2001). The absence of older, high Y cores in the matrix monazite suggests that older, high Y monazite not shielded within the garnet cores were completely consumed during subsequent metamorphic reactions. Two reactions proposed by Pyle and Spear (2003) may account for this observation. First, garnet and high Y monazite were produced in the presence of xenotime (mineral abbreviations after Kretz, 1983):

$$\mathrm{Chl} + \mathrm{Qtz} + \mathrm{Bt} + \mathrm{Pl} + \mathrm{Xno} \rightleftharpoons \mathrm{Grt} + \mathrm{Ms} + \mathrm{Mnz}_{[\text{high Y}]} + \mathrm{Ap} \quad (1)$$

But after xenotime was exhausted, monazite switched to the reactant side and was consumed to produce more garnet, except for those included within garnet:

$$\mathrm{Chl} + \mathrm{Qtz} + \mathrm{Bt} + \mathrm{Pl} + \mathrm{Mnz}_{[\text{high Y}]} \rightleftharpoons \mathrm{Ms} + \mathrm{Ap} + \mathrm{Grt} \quad (1a)$$

Bea and Montero (1999) have also suggested that once xenotime is exhausted, continued garnet growth would obtain Y from other sources that include monazite via melt enhanced dissolution–recrystallization processes. From this point on, xenotime is interpreted to be absent from the reactions proposed below because it was not found to be present in DG38a.

The monazite included in kyanite has a similar Y content (~3500 ppm; Fig. 8b) as the low Y cores assigned to Group 1 (Table 3, excluding spot 3 of Mnz12). Prior to the initial production of kyanite, the low Y monazite found in the matrix grains may have grown during the staurolite—in reaction that consumes garnet (see Pyle et al., 2001):

$$\mathrm{Grt} + \mathrm{Chl} + \mathrm{Ms} \pm \mathrm{Ap} \rightleftharpoons \mathrm{St} + \mathrm{Bt} + \mathrm{Pl} + \mathrm{Mnz}_{[\text{low Y}]} + \mathrm{Qtz} + \mathrm{H_2O} \quad (2)$$

Assuming reaction (2) is responsible for production of the low Y monazite cores of DG38a, it would be constrained to be at least as old as 144.4±4.4 Ma based on the oldest $^{208}Pb/^{232}Th$ SHRIMP age for low Y core found in Mnz9 (Fig. 6, Tables 2 and 3). In Mnz9, the embayment of the oldest low Y core by the younger (ca. 126 Ma) intermediate Y zone indicates that reactions involving monazite at this time involved resorption–reprecipitation. Perhaps consumption of the low Y monazite core occurred during the kyanite—in reaction that involves renewed garnet growth, forcing the consumption of monazite:

$$\mathrm{St} + \mathrm{Pl} + \mathrm{Ms} + \mathrm{Qtz} + \mathrm{Mnz}_{[\text{low Y}]} \rightleftharpoons \mathrm{Grt} + \mathrm{Ky} + \mathrm{Bt} + \mathrm{Ap} + \mathrm{H_20} \quad (3)$$

Staurolite is absent in DG38a, but is not thought to be compositionally controlled because it is found at lower metamorphic grade in the same lithology further to the east. According to the NaKFMASH petrogenetic grid of Spear et al. (1999), the minimum *P–T* constraints for the staurolite-out reaction within the kyanite field are ~7.4 kbar and 675 °C. Once staurolite was exhausted, the renewed growth of ca. 126 Ma monazite with intermediate Y composition, may have progressed by a reaction similar to that proposed by Pyle and Spear (2003; reaction (6)) for near isobaric heating:

$$\mathrm{Grt} + \mathrm{Ms} + \mathrm{Ap} \rightleftharpoons \mathrm{Ky} + \mathrm{Bt} + \mathrm{Mnz}_{[\text{intermediate Y}]} \quad (4)$$

The youngest, high Y rims are interpreted to have formed upon cooling and melt crystallization postdating the peak of metamorphism. The following two reactions were written assuming the kyanite-bearing assemblage of DG38a is a higher-pressure proxy to the cordierite-bearing assemblage described by Pyle and Spear (2003; reactions (4) and (5)):

$$\mathrm{Grt} + \mathrm{Kfs} + \mathrm{Melt} \rightleftharpoons \mathrm{Ky} + \mathrm{Bt} + \mathrm{Qtz} + \mathrm{Pl} + \mathrm{Mnz}_{[\text{high Y}]} \quad (5a)$$

and/or

$$\mathrm{Ky} + \mathrm{Melt} \rightleftharpoons \mathrm{Qtz} + \mathrm{Pl} + \mathrm{Ms} + \mathrm{Mnz}_{[\text{high Y}]} \quad (5b)$$

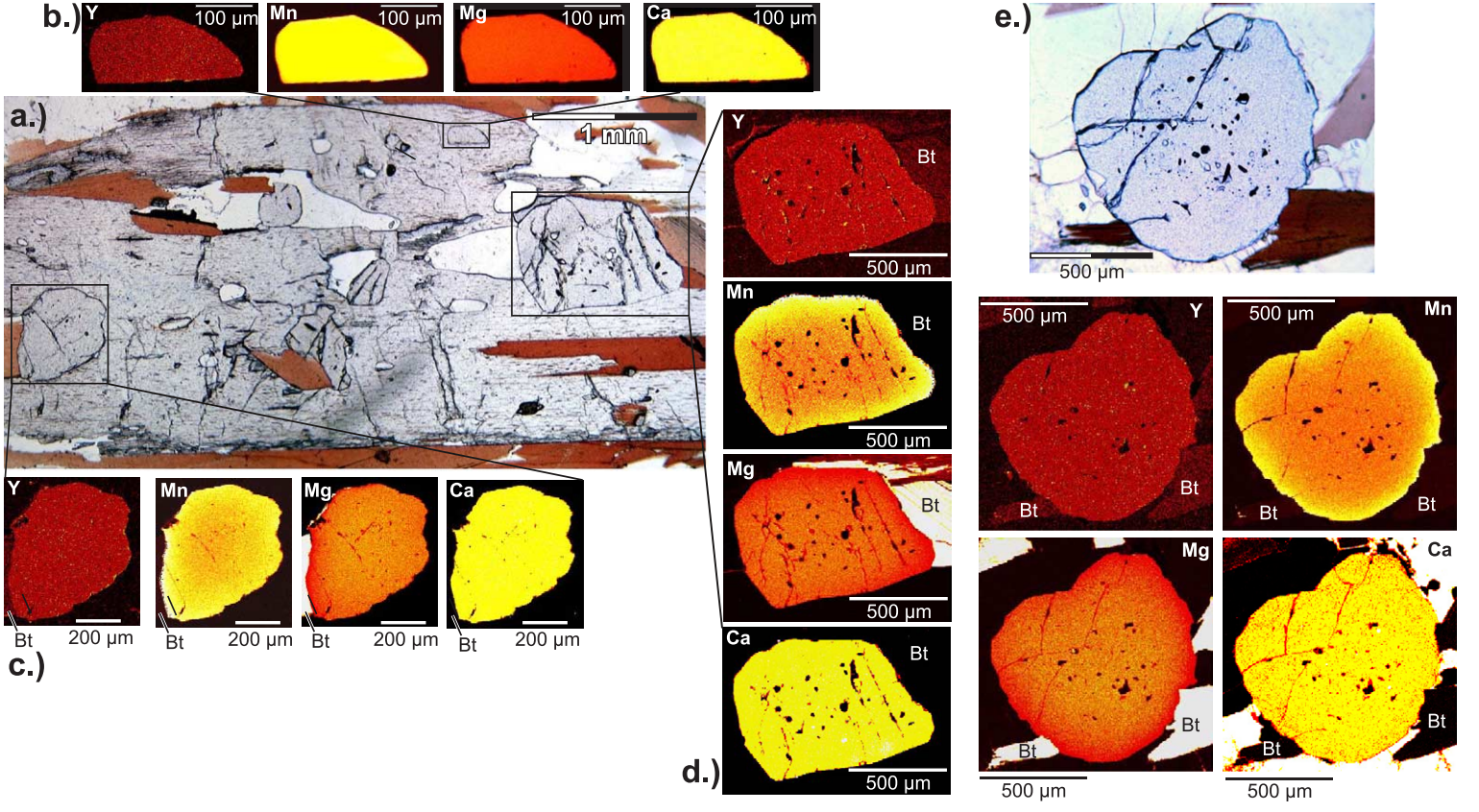

Fig. 10. (a) Photomicrograph from Fig. 2c. (b)–(d) Y, Mn, Mg, and Ca elemental X-ray maps of garnet shown in (a), as outlined by box inset. Brighter colors (yellow to white) represent higher concentrations vs. darker colors (orange and red). (e) Garnet of Fig. 2d, with Y, Mn, Mg, and Ca maps. Note: the I/O levels and contrast were adjusted to emphasize zoning; thus, the colors only give qualitative assessment of element concentration for individual maps. (For interpretation of the references to colour in this figure legend, the reader is referred to the web version of this article.)

The reverse, prograde direction of these reactions require pressures of ≥8 kbar and temperatures of >700 °C using the petrogenetic grid of Spear et al. (1999), which are higher than the average estimates provided by Ghent et al. (1979, 1982, 1983) or Leatherbarrow (1981). However, *P–T* estimates for samples 7–8 of Ghent et al. (1982) near Warsaw Mt., and nearest DG38a, yielded a *P–T* of 8.3 kbar and 740 °C. Interestingly, reaction (5a) may account for the inclusion of young ca. 83–73 Ma monazite in kyanite documented by Crowley et al. (2000) 18 km to the northwest of this study, whereas, reaction (5b) may account for the highly resorbed kyanite observed in DG38a (Fig. 2a and c) and the late cross-cutting muscovite within the leucosome.

Four garnet grains in the thin section of Fig. 2a were mapped for Ca, Mg, Mn, and Y (Fig. 10) to check for the presence of chemical zoning that may have been associated with episodes of growth and resorption. The Ca maps are mostly uniform. Garnet not completely included in kyanite display a rimward Mn kick accompanied by a more diffuse decrease in Mg (Fig. 10c–e) characteristic of retrograde dissolution (see Kohn and Spear, 2000; Kohn and Malloy, 2003). The cores of these grains show a uniform distribution of Ca, Mg, and Mn, as does the smaller, elongated garnet included within kyanite (Fig. 10b), which was shielded from the retrograde dissolution that affected the matrix grains. These observations suggest that prograde zoning of Ca, Mg, and Mn in the garnet homogenized during peak metamorphism (≥740 °C, ≥8 kbar); consequently, the observed Mn–Mg zoning provides insight only into late retrograde dissolution.

The Y maps also demonstrate a lack of discernable zoning (Fig. 10b–e), at least at the resolution of X-ray mapping undertaken in this particular case (current=400 nA; 120 ms counting time; 4 μm steps). Perhaps the Y zones within the garnet were below the threshold of resolution attempted in the analysis. Garnet can accommodate several thousand ppm Y (see Pyle and Spear, 2000b and references therein), and the total volume of garnet in metapelites dwarfs both monazite and xenotime. As such, the breakdown of xenotime and/or monazite may not manifest itself as a noticeable jump in Y, if there is one, unless analyzed at very high resolution.

Another limitation of the above reactions is the lack of consideration given to the role of Th, a major constituent of monazite, and the accessory minerals involved in the contribution or depletion of Th during metamorphism. Thorium silicates, such as allanite (see Smith and Barreiro, 1990; Wing et al., 2003), thorite, and huttonite, Th oxides (thorianite), and other Th phosphates (e.g., cheralite, brabantite; Förster, 1998), likely play an important role concerning the Th budget during metamorphism (see Bea and Montero, 1999, and references therein). Furthermore, other major and/or trace elements may be better for discerning age domains within monazite in rocks with a different bulk chemistry, mineralogy, and pressure–temperature history. These issues are poorly understood, especially in upper amphibolite- to granulite-facies rocks, and require a great deal more study.

Lastly, the results presented above indicate that growth and resorption of metamorphic monazite in this sample spanned 60 to 70 Ma. This supports other geochronologic, petrologic, and structural data for the region that indicate metamorphism and deformation were strongly diachronous, whose age and intensity were, in large part, a function of structural level (e.g., Parrish, 1995; Crowley et al., 2000; Gibson, 2003; Gibson et al., 2003). Further examination of the implications these data to regional geology and metamorphic processes is beyond the scope of this paper, but will be presented in future contributions (Gibson et al., in preparation).

6. Conclusions

The most significant contribution of this study is the clear link that has been established between Y zones of relative depletion or enrichment in metamorphic monazite and age domains as revealed by EMP chemical mapping coupled with in situ SHRIMP analysis. The Y maps provided the best indication of growth and/or recrystallization domains, and were critical for targeting SHRIMP analysis because these relationships were not always clear in BSE, U, and Th images. Moreover, the Y domains consistently correlated with distinct age domains, with up to three or more present in some crystals that ranged in age between ca. 144 and 73 Ma. These data clearly demonstrate that multiple age domains within metamorphic monazite are the cause of the age dispersion

produced in the ID-TIMS analysis. As such, this study adds to a growing body of evidence that points to the significance of multiple age domains within single monazite crystals from medium to high-grade metamorphic terranes. This has significant implications for previous studies that relied upon geochronological techniques such as isotope dilution and linear regressions through discordant data to date metamorphic monazite. Problems related to bulk mixing of multiple age domains combined with isotopic complexities such as unsupported ^{206}Pb might be irreconcilable or erroneously interpreted. Future studies should bear this in mind when deciding on an approach to date monazite to constrain the timing of metamorphism. This does not preclude using ID-TIMS for analyzing metamorphic monazite. Analysis of carefully characterized grain fragments imaged by BSE and/or chemical mapping could yield highly precise and meaningful data, but should be interpreted with caution. If possible, these data should be accompanied by in situ analysis (e.g., EMP, LA-MC-ICPMS, SHRIMP).

The recognition of the link between age domains and Y zones in monazite also has important implications for correlating the ages with major metamorphic reactions. Recent studies have investigated the interaction between accessory and major phases in pelites throughout a metamorphic event and, more specifically, the partitioning of Y between phases such as garnet, monazite, and xenotime (e.g., Bea and Montero, 1999; Foster et al., 2000, 2002; Pyle et al., 2001; Pyle and Spear, 2003). They have established that garnet exerts considerable control over the Y budget available during metamorphism in pelitic rocks. Production and consumption of monazite is sensitive to the availability of Y and is reflected internally in preserved Y zones; data from this study appear to support these interpretations. As such, the precise ages of Y domains within monazite provided by SHRIMP analysis were tentatively correlated with metamorphic reactions involving garnet. However, these reactions lack rigorous thermodynamic modeling associated with quantitative measurements of major and trace elements and are considered speculative. Nevertheless, they provide testable hypotheses that can be considered in a more regional context and have created a framework around which future studies can be shaped.

Acknowledgments

This work was funded by NSERC operating grants held by Sharon Carr and Richard Brown. The J.C. Roddick Ion Microprobe Lab at the GSC is acknowledged for providing access to the facility and assistance in the acquisition and reduction of the U–Th–Pb SHRIMP data. The UMass microprobe lab is thanked for high-quality X-ray elemental mapping of the monazite grains. Insightful discussions with Joseph Pyle and Mike Williams regarding the metamorphic reactions proposed in this paper are greatly appreciated. Lastly, this contribution was greatly improved, thanks to constructive reviews, by Ingo Braun and Daniela Rubatto. Roberta Rudnick is thanked for the excellent editorial handling of the manuscript. **[RR]**

References

Armstrong, R.L., Parrish, R.R., Van der Heyden, P., Scott, K., Runkle, D., Brown, R.L., 1991. Early Proterozoic basement exposures in the southern Canadian Cordillera: core gneiss of Frenchman Cap, Unit I of the Grand Forks Gneiss, and the Vaseaux Formation. Can. J. Earth Sci. 28 (8), 1169–1201.

Bea, F., 1996. Residence of REE, Y, Th and U in granites and crustal protoliths; implications for the chemistry of crustal melts. J. Petrol. 37 (3), 521–552.

Bea, F., Montero, P., 1999. Behavior of accessory phases and redistribution of Zr, REE, Y, Th, and U during metamorphism and partial melting of metapelites in the lower crust: an example from the Kinzigite Formation of Ivrea–Verbano, NW Italy. Geochim. Cosmochim. Acta 63 (7–8), 1113–1153.

Bearden, J.A., 1964. X-ray Wavelengths. U.S. Atomic Energy Commission, Oak Ridge, TN. Report NYO 10586.

Bingen, B., Demaiffe, D., Hertogen, J., 1996. Redistribution of rare earth elements, thorium, and uranium over accessory minerals in the course of amphibolite to granulite-facies metamorphism—the role of apatite and monazite in orthogneisses from Southwestern Norway. Geochim. Cosmochim. Acta 60 (8), 1341–1354.

Braun, I., Montel, J.-M., Nicollet, C., 1998. Electron microprobe dating of monazites from high-grade gneisses and pegmatites of the Kerala khondalite belt, southern India. Chem. Geol. 146 (1–2), 65–85.

Brown, R.L., Tippett, C.R., 1978. The Selkirk fan structure of the southeastern Canadian Cordillera. Geol. Soc. Amer. Bull. 89, 548–558.

Brown, R.L., McNicoll, V.J., Parrish, R.R., Scammell, R.J., 1992. Middle Jurassic plutonism in the Kootenay Terrane, northern Selkirk Mountains, British Columbia. Pap. Geol. Surv. Can. 91–2, 135–141.

Brown, R.L., Beaumont, C., Willett, S.D., 1993. Comparison of the Selkirk fan structure with mechanical models: implications for interpretation of the southern Canadian Cordillera. Geology 21 (11), 1015–1018.

Cherniak, D.J., Watson, E.B., Grove, M., Harrison, T.M., 2002. Pb diffusion in monazite. Abstr. Programs Geol. Soc. Am., Denver 34 (6), 311.

Cocherie, A., Legendre, O., Peucat, J.J., Kouamelan, A.N., 1998. Geochronology of polygenetic monazites constrained by in situ electron microprobe Th–U–total lead determination: implications for lead behaviour in monazite. Geochim. Cosmochim. Acta 62 (14), 2475–2497.

Colpron, M., Logan, J.M., Gibson, G., Wild, C.J., 1995. Geology and Mineral Occurrences of the Goldstream River Area, Northern Selkirk Mountains (82M/9 and part of 10). British Columbia Ministry of Energy, Mines and Petroleum Resources, Map 1995-2, scale 1:50,000.

Colpron, M., Price, R.A., Archibald, D.A., Carmichael, D.M., 1996. Middle Jurassic exhumation along the western flank of the Selkirk fan structure: thermobarometric and thermochronometric constraints from the Illecillewaet synclinorium, southeastern British Columbia. Geol. Soc. Amer. Bull. 108 (11), 1372–1392.

Compston, W., Williams, I.S., Kirschvink, J.L., Zhang, Z., Ma, G., 1992. Zircon U–Pb ages for the Early Cambrian time-scale. J. Geol. Soc. 149 (2), 171–184.

Crowley, J.L., 1999. U–Pb geochronologic constraints on Paleoproterozoic tectonism in the Monashee complex, Canadian Cordillera: elucidating an overprinted geologic history. Geol. Soc. Amer. Bull. 111 (4), 560–577.

Crowley, J.L., Ghent, E.D., 1999. An electron microprobe study of the U–Th–Pb systematics of metamorphosed monazite: the role of Pb diffusion versus overgrowth and recrystallization. Chem. Geol. 157 (3–4), 285–302.

Crowley, J.L., Ghent, E.D., Carr, S.D., Simony, P.S., Hamilton, M.A., 2000. Multiple thermotectonic events in a continuous metamorphic sequence, Mica Creek area, southeastern Canadian Cordillera. Geol. Mater. Res. 2 (2), 1–45.

DeWolf, C.P., Belshaw, N.S., O'Nions, R.K., 1993. A metamorphic history from micron-scale $^{207}Pb/^{206}Pb$ chronometry of Archean monazite. Earth Planet. Sci. Lett. 120 (3–4), 207–220.

Digel, S.G., Ghent, E.D., Carr, S.D., Simony, P.S., 1998. Early Cretaceous kyanite–sillimanite metamorphism and Paleocene sillimanite overprint near Mount Cheadle, southeastern British Columbia: geometry, geochronology, and metamorphic implications. Can. J. Earth Sci. 35 (9), 1070–1087.

Ferry, J.M., 2000. Patterns of mineral occurrence in metamorphic rocks. Am. Mineral. 85 (11–12), 1573–1588.

Förster, H.-J., 1998. The chemical composition of REE-Y-Th-U-rich accessory minerals in peraluminous granites of the Erzgebirge-Fichtelgebirge region, Germany; Part II, Xenotime. Am. Mineral. 83, 1302–1315.

Foster, G., Kinny, P., Vance, D., Prince, C., Harris, N., 2000. The significance of monazite U–Th–Pb age data in metamorphic assemblages; a combined study of monazite and garnet chronometry. Earth Planet. Sci. Lett. 181, 327–340.

Foster, G., Gibson, H.D., Parrish, R.R., Horstwood, M., Fraser, J., Tindle, A., 2002. Textural, chemical and isotopic insights into the nature and behaviour of metamorphic monazite. Chem. Geol. 191 (1–3), 183–207.

Ghent, E.D., Robbins, D.B., Stout, M.Z., 1979. Geothermometry, geobarometry, and fluid compositions of metamorphosed calc-silicates and pelites, Mica Creek, British Columbia. Am. Mineral. 64, 874–885.

Ghent, E.D., Knitter, C.C., Raeside, R.P., Stout, M.Z., 1982. Geothermometry and geobarometry of pelitic rocks, upper kyanite and sillimanite zones, Mica Creek area, British Columbia. Can. Mineral. 20 (3), 295–305.

Ghent, E.D., Stout, M.Z., Raeside, R.P., 1983. Plagioclase–clinopyroxene–garnet–quartz equilibria and the geobarometry and geothermometry of garnet amphibolites from Mica Creek, British Columbia. Can. J. Earth Sci. 20 (5), 699–706.

Gibson, H.D., 2003. Structural and thermal evolution of the northern Selkirk Mountains, southeastern Canadian Cordillera: tectonic development of a regional-scale composite structural fan. PhD Thesis. Carleton University, Canada.

Gibson, H.D., Brown, R.L., Carr, S.D., 2003. Tectonic evolution of the Selkirk fan: a composite Middle Jurassic–Cretaceous structure, northern Selkirk Mountains, southeastern Canadian Cordillera. Geol. Assoc. Can. - Mineral. Assoc. Can. Annual Meeting, Abstracts on CD vol. 28, #401, 2003.

Gibson, H.D., Brown, R.L., Carr, S.D., (in press). U-Th-Pb geochronologic constraints on the structural evolution of the Selkirk fan, northern Selkirk Mountains, southeastern British Columbia. J. Struc. Geol.

Gibson, H.D., Brown, R.L., Carr, S.D., (in preparation). Tectonic evolution of the Selkirk fan: a composite Middle Jurassic–Cretaceous structure, northern Selkirk Mountains, southern Canadian Cordillera. Tectonics.

Goldstein, J.I., Newbury, D.E., Echlin, P., Joy, D.C., Fiori, C., Lifshin, E., 1981. Scanning Electron Microscopy and X-ray Microanalysis: a Text for Biologists, Materials Scientists, and Geologists. Plenum Press, New York.

Goncalves, P., Williams, M.L., Jercinovic, M.J., (in press). Electron microprobe age mapping of monazite. Am. Mineral.

Harrison, T.M., McKeegan, K.D., LeFort, P., 1995. Detection of inherited monazite in the Manaslu leucogranite by $^{208}Pb/^{232}Th$ ion microprobe dating: crystallization age and tectonic implications. Earth Planet. Sci. Lett. 133 (3–4), 271–282.

Hawkins, D.P., Bowring, S.A., 1999. U–Pb monazite, xenotime and titanite geochronological constraints on the prograde to post-peak metamorphic thermal history of Paleoproterozoic migmatites from the Grand Canyon, Arizona. Contrib. Mineral. Petrol. 134, 150–169.

Heaman, L., Parrish, R., 1991. U–Pb geochronology of accessory minerals. In: Heaman, L., Ludden, J.N. (Eds.), Applications of Radiogenic Isotope Systems to Problems in Geology, Short Course Series vol. 19. Mineral. Assoc. Can., Toronto, pp. 59–100.

Kingsbury, J.A., Miller, C.F., Wooden, J.L., Harrison, T.M., 1993. Monazite paragenesis and U–Pb systematics in rocks of the eastern Mojave Desert, California, USA: implications for thermochronometry. Chem. Geol. 110 (1–3), 147–167.

Kohn, M.J., Malloy, M.A., 2003. Formation of monazite via prograde metamorphic reactions among common silicates:

implications for age determinations. Geochim. Cosmochim. Acta 68 (1), 101–113.
Kohn, M.J., Spear, F.S., 2000. Retrograde net transfer reaction insurance for pressure–temperature estimates. Geology 28 (12), 1127–1130.
Kretz, R., 1983. Symbols for rock-forming minerals. Am. Mineral. 68, 277–279.
Leatherbarrow, R.W., 1981. Metamorphism of pelitic rocks from the northern Selkirk Mountains, southeastern British Columbia. PhD Thesis. Carleton University, Canada.
Leatherbarrow, R.W., Brown, R.L., 1978. Metamorphism of the northern Selkirk Mountains, British Columbia. Pap. Geol. Surv. Can. 78-1A, 81–82.
Ludwig, K.R., 2001. Isoplot/Ex version 2.49: a geochronological toolkit for Microsoft Excel. Berkley Geochronology Center.
Monger, J.W.H., Price, R.A., Tempelman-Kluit, D.J., 1982. Tectonic accretion and the origin of the two major metamorphic and plutonic welts in the Canadian Cordillera. Geology 10, 70–75.
Overstreet, W.C., 1967. The geological occurrence of monazite. U.S. Geol. Surv. Prof. Pap. 530, 327.
Pan, Y.M., 1997. Zircon- and monazite-forming metamorphic reactions at Manitouwadge, Ontario. Can. Mineral. 35, 105–118.
Parkinson, D., 1991. Age and isotopic character of early Proterozoic basement gneisses in the southern Monashee complex, southeastern British Columbia. Can. J. Earth Sci. 28 (8), 1159–1168.
Parrish, R.R., 1987. An improved micro-capsule for zircon dissolution in U–Pb geochronology. Chem. Geol. 66, 99–102.
Parrish, R.R., 1990. U–Pb dating of monazite and its application to geological problems. Can. J. Earth Sci. 27 (11), 1431–1450.
Parrish, R.R., 1995. Thermal evolution of the southeastern Canadian Cordillera. Can. J. Earth Sci. 32 (10), 1618–1642.
Parrish, R.R., Krogh, T.E., 1987. Synthesis and purification of 205Pb for U–Pb geochronology. Chem. Geol. 66, 103–110.
Parrish, R.R., Roddick, J.C., Loveridge, W.D., Sullivan, R.W., 1987. Uranium–lead analytical techniques at the geochronology laboratory. Pap. Geol. Surv. Can. 87-2, 3–7.
Parrish, R.R., Carr, S.D., Parkinson, D.L., 1988. Eocene extensional tectonics and geochronology of the southern Omineca Belt, British Columbia and Washington. Tectonics 7 (2), 181–212.
Perkins, M.J., 1983. Structural geology and stratigraphy, Big Bend of the Columbia river, Selkirk Mountains, British Columbia. PhD Thesis. Carleton University, Canada.
Poitrasson, F., Bland, D.J., Chenery, S., 1996. Contrasted monazite hydrothermal alteration mechanisms and their geochemical implications. Earth Planet. Sci. Lett. 146 (1–4), 79–96.
Poitrasson, F., Chenery, S., Shepherd, T.J., 2000. Electron microprobe and LA-ICP-MS study of monazite hydrothermal alteration: implications for U–Th–Pb geochronology and nuclear ceramics. Geochim. Cosmochim. Acta 64 (19), 3283–3297.
Poulton, T.P., Simony, P.S., 1980. Stratigraphy, sedimentology, and regional correlation of the Horsethief Creek Group (Hadrynian, Late Precambrian) in the northern Purcell and Selkirk Mountains, British Columbia. Can. J. Earth Sci. 17 (12), 1708–1724.
Price, R.A., Mountjoy, E.W., 1970. Geological structure of the Canadian Rocky Mountains between Bow and Athabasca Rivers—a progress report. In: Wheeler, J.O. (Ed.), Structure of the Southern Canadian Cordillera, Spec. Pap. Geol. Assoc. Can. vol. 6, pp. 7–25.
Pyle, J.M., Spear, F.S., 2000a. Accessory-phase paragenesis in low-P migmatites, Chesham Pond nappe, SE new Hampshire. Abstr. Programs - Geol. Soc. Am., Boulder, A297.
Pyle, J.M., Spear, F.S., 2000b. An empirical garnet (YAG)–xenotime thermometer. Contrib. Mineral. Petrol. 138, 51–58.
Pyle, J.M., Spear, F.S., 2003. Four generations of accessory-phase growth in low-pressure migmatites from SW New Hampshire. Am. Mineral. 88, 338–351.
Pyle, J.M., Spear, F.S., Rudnick, R.L., McDonough, W.F., 2001. Monazite–xenotime–garnet equilibrium in metapelites and a new monazite–garnet thermometer. J. Petrol. 42 (11), 2083–2107.
Raeside, R.P., Simony, P.S., 1983. Stratigraphy and deformational history of the Scrip Nappe, Monashee Mountains, British Columbia. Can. J. Earth Sci. 20 (4), 639–650.
Read, P.B., Brown, R.L., 1981. Columbia River fault zone: southeastern margin of the Shuswap and Monashee complexes, southern British Columbia. Can. J. Earth Sci. 18 (7), 1127–1145.
Roddick, J.C., 1987. Generalized numerical error analysis with applications to geochronology and thermodynamics. Geochim. Cosmochim. Acta 51, 2129–2135.
Roddick, J.C., Loveridge, W.D., Parrish, R.R., 1987. Precise U/Pb dating of zircon at the sub-nanogram Pb level. Chem. Geol. 66, 111–121.
Rubatto, D., Williams, I.S., Buick, I.S., 2001. Zircon and monazite response to prograde metamorphism in the Reynolds Range, central Australia. Contrib. Mineral. Petrol. 140, 458–468.
Scammell, R.J., 1993. Mid-Cretaceous to Tertiary thermotectonic history of former mid-crustal rocks, southern Omineca belt, Canadian Cordillera. PhD Thesis. Queen's University, Canada.
Schärer, U., 1984. The effect of initial 230Th disequilibrium on young U–Pb ages: the Makalu case, Himalaya. Earth Planet. Sci. Lett. 67, 191–204.
Sevigny, J.H., Parrish, R.R., Ghent, E.D., 1989. Petrogenesis of peraluminous granites, Monashee Mountains, southeastern Canadian Cordillera. J. Petrol. 30 (3), 557–581.
Sevigny, J.H., Parrish, R.R., Donelick, R.A., Ghent, E.D., 1990. Northern Monashee Mountains, Omineca Crystalline Belt, British Columbia: timing of metamorphism, anatexis, and tectonic denudation. Geology 18, 103–106.
Shannon, R.D., 1976. Revised effective ionic radii and systematic studies of interatomic distances in halides and chalcogenides. Acta Crystallogr. A32, 751–767.
Shaw, D., 1980. A concordant uranium–lead age for zircons in the Adamant Pluton, British Columbia. Pap. Geol. Surv. Can. 80-1C, 243–246.
Simony, P.S., Ghent, E.D., Craw, D., Mitchell, W., Robbins, D.B., 1980. Structural and metamorphic evolution of the northeast flank of Shuswap complex, southern Canoe River area, British Columbia. Geol. Soc. Am., Mem. 153, 445–461.
Smith, H.A., Barreiro, B., 1990. Monazite U–Pb dating of staurolite grade metamorphism in pelitic schists. Contrib. Mineral. Petrol. 105, 602–615.

Smith, H.A., Giletti, B.J., 1997. Lead diffusion in monazite. Geochim. Cosmochim. Acta 61 (5), 1047–1055.

Spear, F.S., Parrish, R.R., 1996. Petrology and cooling rates of the Valhalla Complex, British Columbia, Canada. J. Petrol. 37 (4), 733–765.

Spear, F.S., Kohn, M.J., Cheney, J.T., 1999. *P–T* paths from anatectic pelites. Contrib. Mineral. Petrol. 134, 17–32.

Stacey, J.S., Kramers, J.D., 1975. Approximation of terrestrial lead isotope evolution by a two-stage model. Earth Planet. Sci. Lett. 26, 207–221.

Steiger, R.H., Jäger, E., 1977. Subcommission on geochronology: convention on the use of decay constants in geo- and cosmochronology. Earth Planet. Sci. Lett. 36, 359–362.

Stern, R.A., 1997. The GSC sensitive high resolution ion microprobe (SHRIMP): analytical techniques of zircon U–Th–Pb age determinations and performance evaluation. Curr. Res. Geol. Surv. Can. 1997, 1–31.

Stern, R.A., Berman, R.G., 2000. Monazite U–Pb and Th–Pb geochronology by ion microprobe, with an application to in situ dating of an Archean metasedimentary rock. Chem. Geol. 172, 113–130.

Stern, R.A., Sanborn, N., 1998. Monazite U–Pb and Th–Pb geochronology by high-resolution secondary ion mass spectrometry. Geol. Surv. Can. Current Research 1998-F, pp. 1–18.

Tera, F., Wasserburg, G.J., 1972. U–Th–Pb systematics in three Apollo 14 basalts and the problem of initial Pb in lunar rocks. Earth Planet. Sci. Lett. 14, 281–304.

Wheeler, J.O., 1963. Rogers pass map-area, British Columbia and Alberta (82N West Half). Pap. Geol. Surv. Can. 62-32, 1–32.

Wheeler, J.O., 1965. Big Bend map-area, British Columbia. Pap. Geol. Surv. Can. 64-32, 1–37.

Wheeler, J.O., McFeely, P., 1991. Tectonic assemblage map of the Canadian Cordillera and adjacent parts of the United States of America. Geol. Surv. Can. Map 1712A, scale 1:2,000,000.

Williams, M.L., Jercinovic, M.J., Terry, M.P., 1999. Age mapping and dating of monazite on the electron microprobe: deconvoluting multistage tectonic histories. Geology 27, 1023–1026.

Wing, B.A., Ferry, J.M., Harrison, T.M., 2003. Prograde destruction and formation of monazite and allanite during contact and regional metamorphism of pelites: petrology and geochronology. Contrib. Mineral. Petrol. 145, 228–250.

York, D., 1969. Least squares fitting of a straight line with correlated errors. Earth Planet. Sci. Lett. 5, 320–324.

Yunxiang, N., Hughes, J.M., Mariano, A.N., 1995. Crystal chemistry of the monazite and xenotime structures. Am. Mineral. 80, 21–26.

Zhu, X.K., O'Nions, R.K., 1999a. Monazite chemical composition: some implications for monazite geochronology. Contrib. Mineral. Petrol. 137 (4), 351–363.

Zhu, X.K., O'Nions, R.K., 1999b. Zonation of monazite in metamorphic rocks and its implications for high temperature thermochronology: a case study from the Lewisian terrain. Earth Planet. Sci. Lett. 171 (2), 209–220.

Zhu, X.K., O'Nions, R.K., Belshaw, N.S., Gibb, A.J., 1997. Significance of in situ SIMS chronometry of zoned monazite from the Lewisian granulites, northwest Scotland. Chem. Geol. 135 (1–2), 35–53.